H. Bhadeshia

Innovations in Ultrahigh-Strength Steel Technology

Edited by

Gregory B. Olson
Northwestern University
Evanston, Illinois

Morris Azrin
U.S. Army Materials Technology Laboratory
Watertown, Massachusetts

and

Edward S. Wright
U.S. Army Materials Technololgy Laboratory
Watertown, Massachusetts

Library of Congress Cataloging in Publication Data

Sagamore Army Materials Research Conference (34th: 1987: Lake George, N.Y.)
Innovations in Ultrahigh - Strength Steel Technology

(Sagamore Army Materials Research Conference proceedings: 34th)
Bibliography:
Includes index.

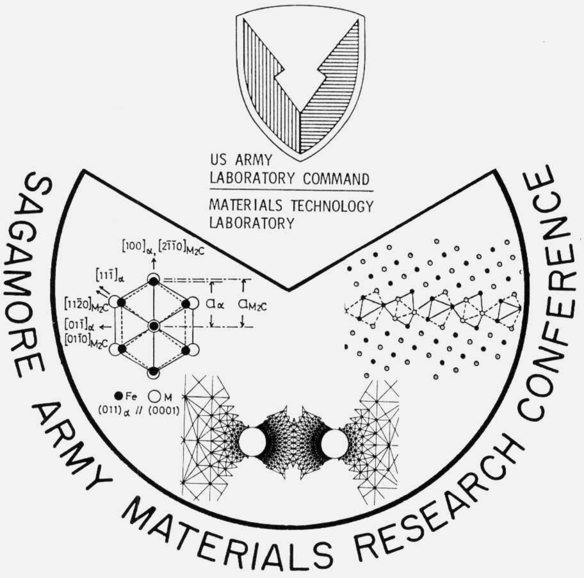

Proceedings of the 34th Sagamore Conference, titled Innovations in Ultrahigh - Strength Steel Technology, held August 30 - September 3, 1987, at Lake George, New York.

34th SAGAMORE CONFERENCE COMMITTEE

Chairmen

EDWARD S. WRIGHT
U.S. Army Materials Technology Laboratory

GREGORY B. OLSON
Northwestern University

Program Director
MORRIS AZRIN
U.S. Army Materials Technology Laboratory

Conference Coordinator
KAREN A. KALOOSTIAN
U.S. Army Materials Technology Laboratory

Program Committee

EDWARD S. WRIGHT
U.S. Army Materials Technology Laboratory

RICHARD CHAIT
U.S. Army Materiel Command

GORDON A. BRUGGEMAN
U.S. Army Materials Technology Laboratory

GEORGE H. BISHOP, JR.
U.S. Army Materials Technology Laboratory

ERIC B. KULA
U.S. Army Materials Technology Laboratory

MORRIS AZRIN
U.S. Army Materials Technology Laboratory

GREGORY B. OLSON
Northwestern University

MORRIS COHEN
Massachusetts Institute of Technology

GEORGE MAYER
Institute for Defense Analyses

ANDREW DIETRICH
U.S. Army Ballistic Research Laboratory

Conference Administration
BATTELLE COLUMBUS DIVISION
505 King Avenue
Columbus, Ohio 43201

Preface

The U.S. Army Materials Technology Laboratory (MTL) has conducted the Annual Sagamore Army Materials Research Conference since 1954. The specific purpose of these conferences is to bring together scientists and engineers from academic institutions, industry, and government for in-depth exploration of subjects of importance to the Department of Defense, the Army, and the scientific community.

The 34th Sagamore Conference addressed "Innovations in Ultrahigh-Strength Steel Technology" in recognition of the continuing vital role of advanced steels in Army systems, and the new scientific opportunities in this field made possible by recent advances in both theory and instrumentation. As a slight departure from the organization of previous Sagamore Conferences, this conference centered on an on-going, multi-institutional university/government/industry research program known as the Steel Research Group (SRG). Originally organized at MIT, the SRG has involved collaboration of Northwestern, Harvard, and Brown Universities, IIT, MTL and Los Alamos National Laboratory, Carpenter, Republic, Bethlehem, and Inland Steel, and General Motors Corporation. The SRG research thrust addressed by the Sagamore Conference focuses the scientific principles of strength, toughness, and hydrogen embrittlement resistance to allow "first-principles" design of a new generation of ultrahigh-strength steels. In addition to the SRG participants, the conference was attended by numerous colleagues whose research impinges directly on the program focus. The exciting exchange of new ideas proved a valuable stimulus to subsequent research.

The period following the conference saw profound changes involving a major realignment of the U.S. Army's materials research effort, unfortunately including the planned closing of the MTL Watertown site, ending a tradition of materials research spanning more than a century and a rare innovative example of a government laboratory exclusively devoted to materials research. The SRG program also underwent a substantial reorganization with Northwestern University replacing MIT as the lead institution, involving a major change in the program sponsorship. The new SRG has emerged more productive than ever, providing not only dramatic advances in fundamental understanding, but pioneering a systems approach to the synthesis of understanding in materials design that serves to define a new concept of materials science. Many of the papers assembled in these proceedings reflect exciting new results recently obtained following approaches stimulated by the conference discussions, and involving a level of integration of new concepts that was only notional at the time of the conference.

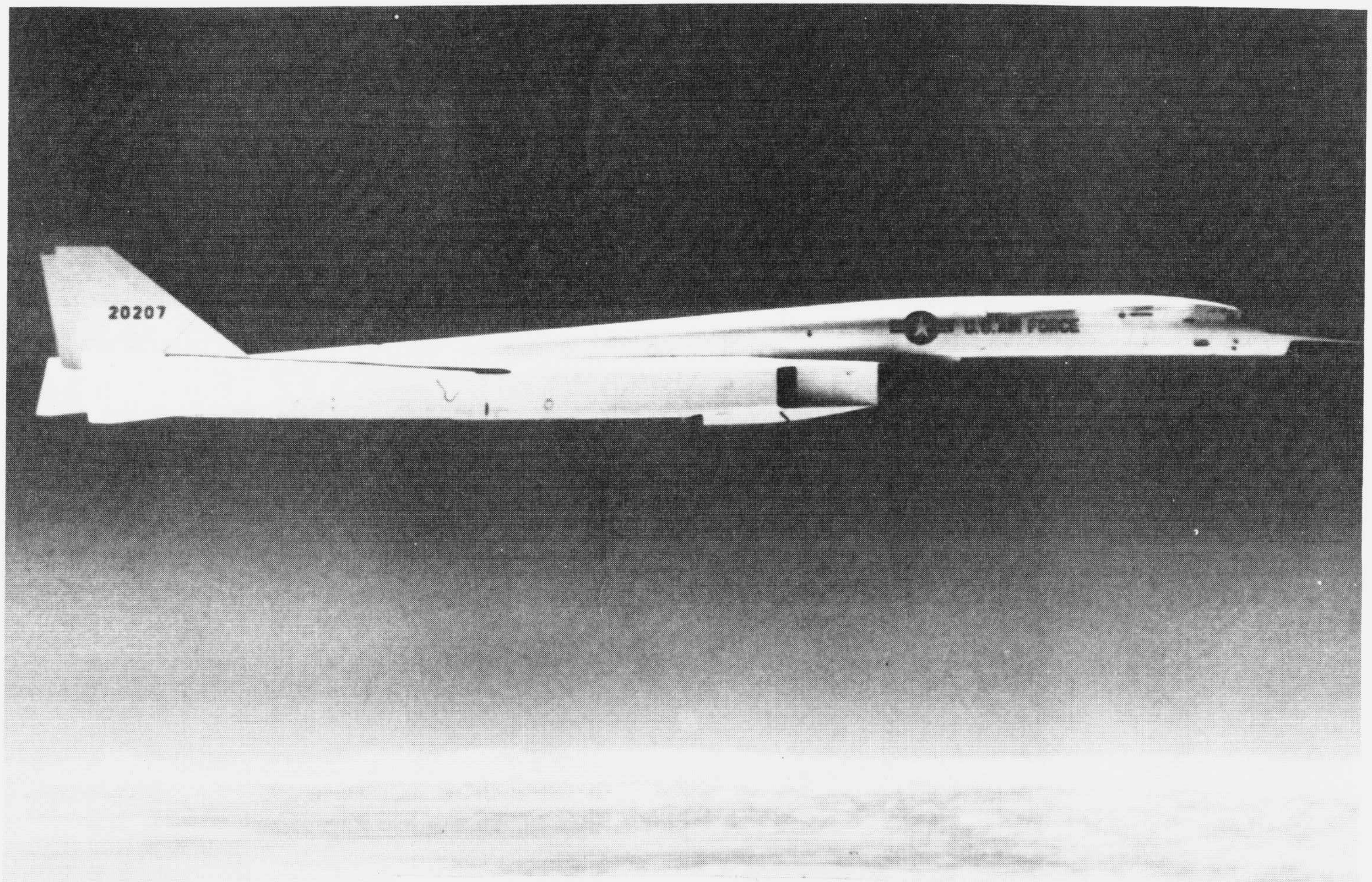

STEEL AIRPLANE: ROCKWELL XB-70

A highpoint of the conference was the banquet lecture of Dr. Neil Paton of Rockwell International - Rocketdyne Division on "Steel in Space" elucidating the role of advanced steels in aerospace applications. While the need for lightweight structures drives the search for alternative low density materials in current design projects such as the National AeroSpace Plane, steels can play a surprisingly important role in some aerospace systems. After describing the criteria that led to the selection of certain alloy steels for the predominant skin materials of Mach 3.0 aircraft (pictured in the frontispiece of this book), Dr. Paton described steel applications in the Space Shuttle ranging from over 200 tons of steel in the solid booster casings to a critical cryogenic bearing application in the main engine fuel and oxidizer turbo pumps. The latter application subsequently inspired a materials design class project at Northwestern University in which emerging concepts from SRG research were integrated in the computer-aided thermodynamics-based conceptual design of a 7-component stainless bearing steel for improved toughness and stress-corrosion resistance, the first example of such a comprehensive material design.

We wish to acknowledge the assistance of Ms. Karen Kaloostian of MTL for all the many arrangements provided before and during the conference. We also wish to acknowledge the technical and logistical assistance of the Metals and Ceramics Information Center operated by Battelle Columbus Division, and the efforts of Mrs. Joan Purvis of Synergic Communication Services, Inc., during the conference, and in assembling these proceedings for publication.

We are deeply saddened by the loss of Professor Gilbert R. Speich of IIT who passed away February 16, 1990, after over three decades of inspired contributions to ferrous metallurgy. Active in both the Sagamore Conference and the SRG program, Professor Speich's pioneering research formed the foundation for much of the ultrahigh-strength steel research reported here. We dedicate this book to his memory.

G.B.Olson
M. Azrin
E.S. Wright

Watertown, MA
March 1990

GILBERT R. SPEICH - A MEMORIAL TRIBUTE

Just as the papers of this Conference were going to press, it was learned with dismay that one of the foremost participants, Gilbert R. Speich, had succumbed to a lingering and grievous illness. He died on 16 February 1990 due to a virulent form of liver disease. Yet, almost to the very end, he remained active and productive, continuing resolutely with his lectures, research, and attendance at technical meetings. Never once did he refer to his inner turmoil.

Gil Speich was a metallurgist's metallurgist by any measure. He received the B.S. degree in Metallurgical Engineering from the Illinois Institute of Technology in 1950, the M.S. degree in Metallurgical Engineering from the University of Wisconsin in 1951, and the Sc.D. degree in Metallurgy from MIT in 1958. Throughout his extensive professional career -- first as a research metallurgist at the U.S. Steel Corporation Research Laboratory and later as Professor and Chairman of the IIT Department of Materials and Metallurgical Engineering -- Gil devoted his primary attention to the physical metallurgy of iron and steel. His accomplishments have been many and widely quoted in the technical literature. Only a few of the highlights can be cited here.

Gil was among the first to investigate the displacive nature of bainitic transformations, and he took advantage of the attendant surface upheavals to measure isothermal growth rates in situ under the optical microscope. He then extended such hot-stage metallography to quantitative observations on structural changes during rapid quenching and also during rapid heating by laser techniques. Gil's ingenuity and thoroughness in research is nicely exemplified by his classic study of precipitate-coarsening kinetics in which he systematically investigated and tied-together all the relevant aspects of the diverse phenomena at play: solubility-limits, interfacial energies of nonspherical particles, thermodynamic driving forces, diffusivities, and quantitative metallography via electron microscopy.

Gil's research on structure/property relationships in ferrous alloys has exerted a major influence on the field. He was one of the leaders in clarifying the nature of dual-phase steels, both by establishing ingenious treatments to vary the operative microstructures and by linking these manifestations to the resulting mechanical properties. In addition, he carried out seminal studies on the tempering of martensitic steels and this, in turn, led to his pioneering development of high-alloy secondary-hardening steels having remarkable combinations of yield strength and fracture toughness. In fact, that advance became the central theme of the present Conference on "Innovations in Ultrahigh-Strength Steel Technology". It turned out to be a most fortunate circumstance for the technical community and posterity that Gil Speich was able to summarize and update his contributions on that subject by giving the lead-off paper on "Secondary Hardening Ultrahigh-Strength Steels", which now appears in this volume.

Sadly, physical metallurgy has now lost one of those rare engineering scientists who are able to excel in bridging the broad spectrum of theory, experiment, and practical purpose. Gilbert Speich epitomized all this with exquisite care, quiet perseverance, and scholarly understanding. As a metallurgist and human being, he touched us all in many wholesome ways, and we are profoundly grateful for it.

Cambridge, Massachusetts
March 1990

Morris Cohen

Contents*

Introduction

Section I: Strengthening

---

* Author(s) and affiliation as indicated on manuscript

Section II: Toughness

IIA: Fracture and Shear Localization

IIB: Transformation Toughening

Section III: Hydrogen Embrittlement Resistance

Appendix

Introduction

OVERVIEW: SCIENCE OF STEEL

G.B. OLSON
Department of Materials Science and Engineering, Northwestern University, Evanston, IL 60208

INTRODUCTION: STEELS AND MATERIALS DESIGN

Steel is the frontier of materials science. More is known about steels than any other class of materials. Paradoxically, despite this position in fundamental understanding, the actual process by which new steels are still developed amounts to the same empiricism which is applied to newer materials for which the alternative of science-based design is not an option. In the arena of empiricism the maturity of steels poses a severe disadvantage in that the "soft ground" has already been explored and empirical development has reached a point of diminishing returns. To compete with newer materials for which traditional empiricism can bring more rapid improvements, there is a pressing need for a better way to develop new steels. Moreover, the ultimate goal of materials science must certainly be the design of superior materials from basic understanding; our very limited ability to truly design materials calls into question the viability of this discipline. This circumstance makes the science of steel a most timely subject: no material is in a better position to be designed from scientific knowledge at the same time that no material is in more need of this approach.

The research reviewed here is based primarily on the Steel Research Group (SRG) program, a multi-institutional university/government/industry interdisciplinary effort directed at the scientific principles for the design of new classes of steels, motivated by specific property objectives of importance to industry. Two key classes of steels have been selected. The major effort reviewed here ("A" Program) is directed at ultrahigh-strength martensitic steels for advanced structural applications, while a smaller effort ("B" Program) is directed at high-strength ferrite-based microalloyed steels for high formability automotive sheet applications. Objectives have been deliberately chosen to represent a sufficiently ambitious advance to require a more fundamental approach to materials design than ever previously attempted.

PROPERTY OBJECTIVES

The performance of a material in service is controlled by a set of properties. Surprisingly, our ability to specify the long list of properties actually required for a given application can be the weakest link in the materials design process. In searching for a model system in which to develop a new approach to design, it is helpful to examine the most demanding applications for which the list of properties one can reasonably request is relatively short. Ultrahigh strength steels for advanced structural applications are an excellent example where primary objectives can be expressed in terms of the three properties of strength, toughness, and hydrogen resistance. If a sufficiently improved combination of these properties can be achieved, other properties such as cost and processability are secondary considerations.

Strength/toughness objectives adopted for the ultrahigh strength steels are depicted in Figure 1 which shows data compiled at MTL representing the typical K_{IC} fracture toughness levels of commercial steels currently in use in applications requiring hardness levels of R_c50 and above. Also indicated are the approximate ultimate tensile strength (UTS) corresponding to each hardness. Marginal fracture toughness and corresponding critical flaw size limit the useable hardness level in structural applications (involving significant tensile loads) to R_c55, with more conservative

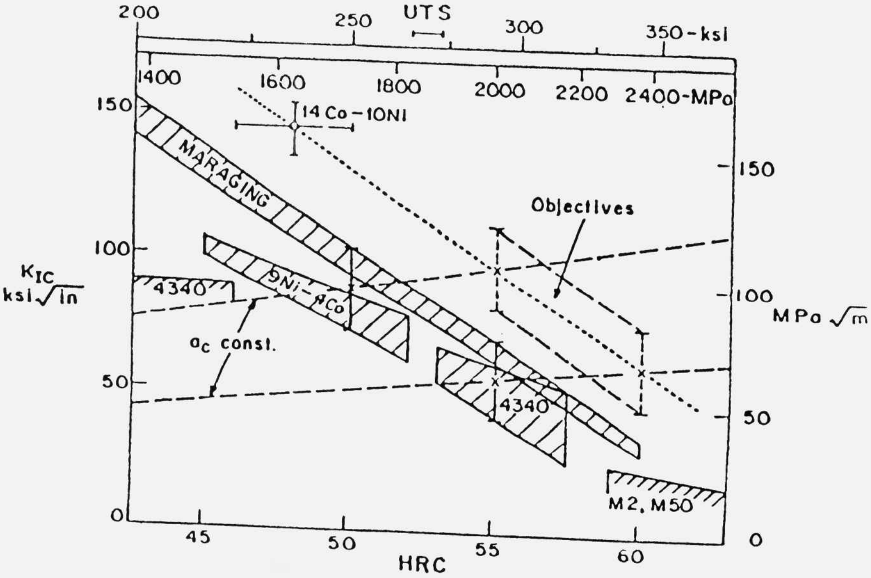

Fig. 1 Typical plane-strain fracture toughness (K_{IC}) vs. Rockwell C hardness (HRC) for commercial ultrahigh-strength steels currently employed in advanced structural applications. Upper scale shows approximate ultimate tensile strength (UTS) with indicated error limit. Strength/toughness objectives depicted allow an advance in useable strength corresponding to 5 points HRC.

applications demanding greater flaw tolerance limited to R_c50. The dashed lines depict contours of constant critical flaw size at a design stress proportional to hardness, identifying the objectives shown to allow a 5 R_c point increase in useable hardness level. The latter corresponds to a substantial strength increment of 50 ksi or 400 MPa. The strength levels thus defined mark the toughness "frontier" of ultrahigh-strength steels; the objectives posed demanding K_{IC} improvements by a factor of 2 at R_c55 and 3 at R_c60.

While low alloy stage-I tempered (ε-carbide strengthened) martensitic steels, exemplified by 4340, still show potential for toughness improvement and are the subject of further study under the SRG program, the new class of steels which has so far demonstrated the highest combinations of strength and toughness is the high alloy secondary-hardening (alloy carbide strengthened) martensitic steels, currently represented by the commercial HY180 and AF1410 steels. At R_c45, HY180 exhibits K_{IC} toughness levels in excess of 230 ksi$\sqrt{in}$, beyond the scale of Figure 1. The higher-strength AF1410 reliably provides a K_{IC} toughness of 140 ksi$\sqrt{in}$ at R_c48 as depicted in Figure 1, while exceptional commercial heats can show 190 ksi$\sqrt{in}$. Expanding this class of steel to the ultrahigh-strength R_c55-60 range offers the greatest potential of meeting our toughness objectives. Moreover, in extending the useable strength of structural steels to R_c60, such secondary hardening steels would overlap with tool steels (represented by M2 and M50 in Figure 1) of interest for bearing and gear applications, thus creating a class of steels with a wide range of potential applications.

Although fracture toughness is an important consideration, a more serious limitation on the reliability of ultrahigh-strength steels is their low resistance to stress-corrosion cracking, which at these strength levels occurs by a hydrogen embrittlement mechanism associated with cathodic charging at the crack tip. At R_c55, the low hydrogen resistance limits the stress corrosion threshold K_{ISCC} to ~10 ksi$\sqrt{in}$. Raising useable strength to the levels depicted in Figure 1 requires major improvements in hydrogen stress-corrosion resistance in order to maintain a K_{ISCC}/K_{IC} ratio of at least 0.5 out to R_c60. As traditional alloy development approaches have produced little change in this property of ultrahigh strength steels in the past decade, the required K_{ISCC} improvements represent the most ambitious objective of the SRG effort, warranting the most interdisciplinary and fundamental approach.

MATERIALS AS SYSTEMS: AN APPROACH TO DESIGN

The central paradigm of materials science is the sequential interrelation of processing, structure, properties, and performance. Although empirical development attempts to bypass elements of this sequence, for example correlating processing and performance without regard to structure/property relations, scientific understanding demands that each link of the sequence be known. Cause-and-effect logic gives a natural direction to this sequence of the form: processing→structure→properties→performance, and from the philosophy of scientific analysis by which we distill simple laws from natural complexity, it it tempting to imagine a materials design process in which predictive theory specifies a composition and processing producing the necessary structure providing the required properties for desired performance. In practice each of these elements and their interrelation is of infinite complexity in real materials, severely compromising our predictive abilities. To usefully synthesize available understanding, we must combine with the scientist's methods of simplifying analysis the engineer's methods for dealing with real complexity, formalized in the "systems" approach (1).

Cyril Smith (2) has expounded on the notion of materials as systems, characterized by a hierarchical structure of interacting microstructural subsystems. Processing and properties can each be likewise described as hierarchies of interactive subsystems, each such subsystem involving important cross-interactions with microstructural subsystems. Morris Cohen (3) has observed that within this interlocking network there is a "reciprocity" such that equally valid to the notion that structure controls properties is the alternative view that properties control structure: our perception of structure is a function of the properties we are attempting to explain. This yields the important principle that knowledge of the relation of a particular component (subsystem) of structure to a property can be used to improve that property without ever requiring the impossible task of characterizing the entire structure. An important aspect of the engineering science of materials is then the discrimination between microstructural components which are actively linked to properties of interest, and inert ingredients such as nonessential evolutionary vestiges which are a common feature of complex systems. As emphasized by Cohen (3,4) this will always involve a blend of predictive theory and empiricism. It is a reasonable expectation that by a combination of predicting the predictable and measuring the measurable we can identify sufficient subsystem interrelations to pose process/structure solutions to property/performance problems, tempered by a certain amount of discouragement from "unknowables" which are beyond our current abilities to predict or measure.

The flow-block diagram of Figure 2 describes the structure of Ni-Co secondary hardening martensitic steels as a hierarchy of microstructural subsystems defined from the viewpoint of combined strength, toughness, and hydrogen resistance, and identifying the stages of processing affecting each. The multicomponent matrix of the steels consists of a lath martensitic microstructure (representing the best class of microstructure for strength/toughness) with a high Ni content for cleavage resistance. Based on the seminal research of Speich (5,6) the Co is used to retard dislocation recovery (which we will later associate with short-range order), which has an important interaction with the strengthening subsystems via heterogeneous nucleation of the M_2C (and MC) carbide strengthening dispersion on the dislocations during tempering. Speich's study of HY180 (6), which formed the basis of the AF1410 development, further showed that an optimum strength/toughness combination is achieved by bringing the alloy carbide precipitation reaction to completion in order to dissolve the relatively coarse transient θ-cementite (Fe_3C) which precipitates earlier and acts as a microvoid nucleation site limiting ductile fracture resistance. The M_2C carbide primarily responsible for secondary hardening is metastable, and high fracture toughness also demands that this metastable reaction reach completion without the nucleation of more stable carbides (M_6C, $M_{23}C_6$) which can precipitate incoherently on interfaces and degrade toughness.

Microvoid nucleation during plastic deformation accelerates ductile fracture through a process of shear localization. Once the precipitation kinetics of competing phases are controlled to achieve a fine strengthening dispersion without unnecessary coarser particles, resistance to microvoid nucleation is ultimately governed by the grain refining dispersion necessary to maintain a sufficiently fine grain size during solution treatment to inhibit competing brittle fracture modes. The grain refining ability of this dispersion is set by the ratio of average particle diameter d to the volume fraction f. Subject to this constraint, toughness enhancement can be sought from an optimization of the geometry and composition of the dispersion (set by earlier processing stages), in order to increase microvoid nucleation resistance.

Further toughening can be achieved through modification of matrix constitutive behavior, the most dramatic example being the incorporation of transformation plasticity from a dispersion of metastable austenite particles precipitated

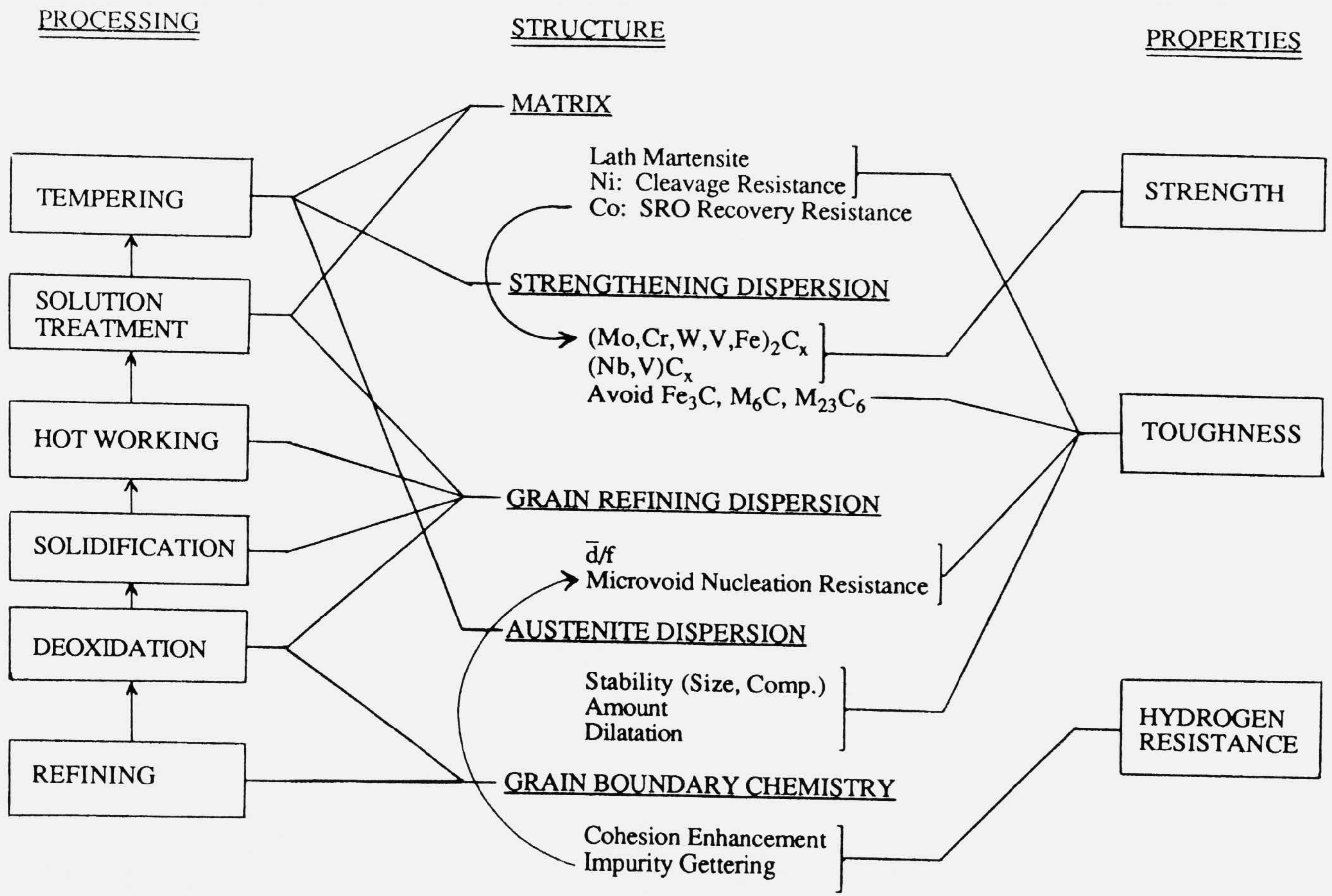

Fig. 2 Flow-block diagram illustrating the interactive hierarchical structure of a Co-Ni secondary hardening martensitic steel from the viewpoint of desired properties.

during tempering. The transformation toughening is sensitive to the particle transformation kinetic stability (controlled by particle size and composition), the amount of dispersed phase, and the magnitude of its transformation dilatation.

Hydrogen stress corrosion cracking in ultrahigh strength martensitic steels occurs by a brittle intergranular cleavage mechanism invariably associated with boundary segregation of embrittling metalloid impurities. The embrittlement appears to be controlled by the chemistry of intrinsic boundary cohesion. Under the SRG program, an interdisciplinary effort is directed at the ultimate application of an electronic-level understanding of intergranular cohesion to the design of grain boundary composition for both enhanced intrinsic cohesion and reduced interaction with hydrogen. A parallel effort explores the use of novel processing techniques to getter embrittling impurities into highly stable compounds, potentially offering the additional toughening benefit of cleaning the interphase boundaries controlling microvoid nucleation.

As is a common feature of systems, the separate optimization of each of the subsystems of Figure 2 poses conflicting objectives. Optimization of the total system demands compromise between subsystems such that local optimizations are highly constrained by the requirements of other subsystems. After reviewing progress in our understanding of the functioning of each of these subsystems, we will examine its application in conceptual designs which effect this compromise.

STRENGTHENING

The strength of overaged precipitation-hardened structures is controlled by the Orowan bypass mechanism for which strength is inversely related to the particle mean free path. For a given amount of precipitating phase, maintaining the highest possible strength at completion of precipitation requires minimization of the final particle size. This is controllable in principle through application of transformation kinetic theory, once theory is properly calibrated by appropriate experiments in the system of interest. It is a fairly recent development that available instrumentation has attained the capabilities required to adequately characterize the fine scale strengthening dispersions of ultrahigh-strength steels.

Results of an ongoing comprehensive study of M_2C carbide precipitation in AF1410 steel are summarized in Figure 3. The figure shows the M_2C carbide particle size, shape, number density, volume fraction, lattice parameters,

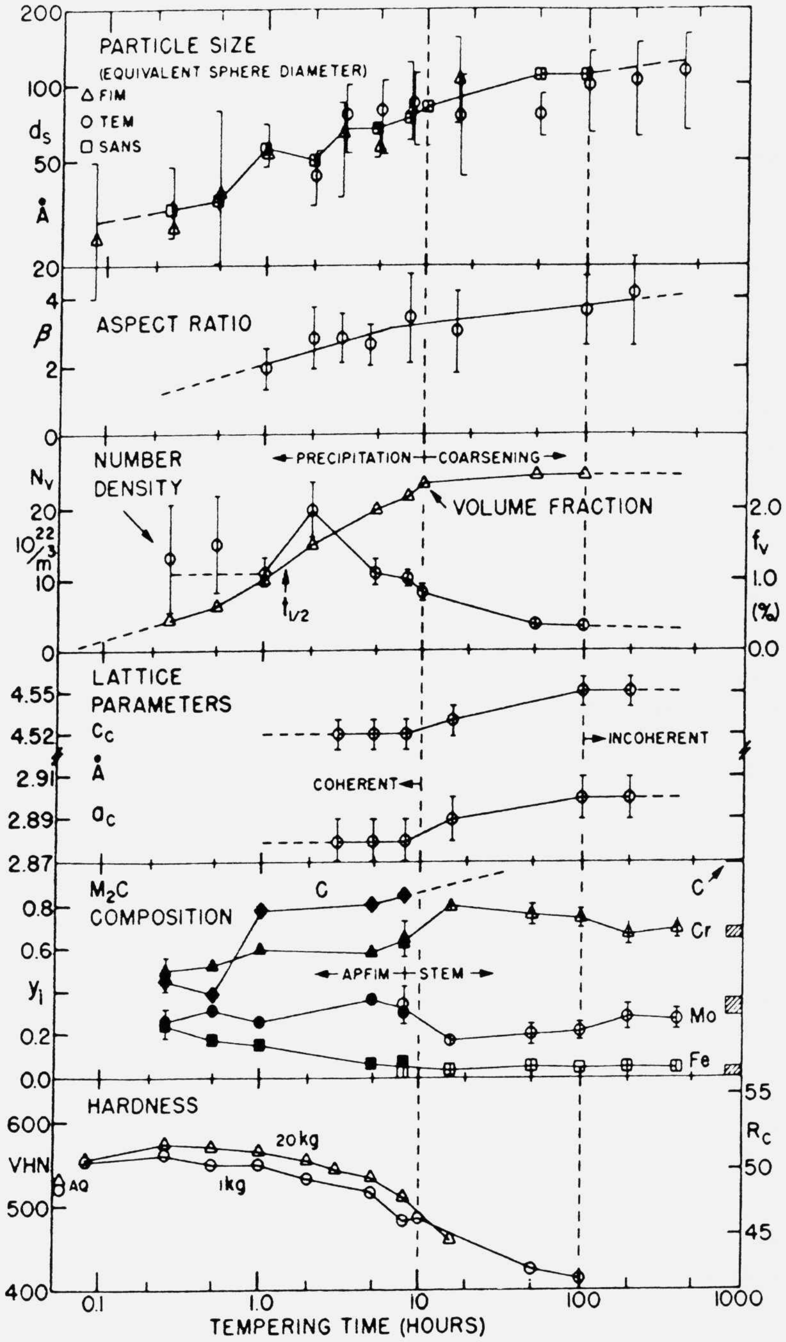

Fig. 3 M_2C carbide precipitation behavior in AF1410 steel vs. tempering time at 510C following 1 hr solution treatment at 830C.

and composition, as well as the steel hardness, all as a function of tempering time at the standard temperature of 510C, following 1 hr solution treatment at the standard austenitizing temperature of 830C. The alloy composition studied is given in Table 1. The average particle size of the rod-shaped carbides is expressed by the diameter, d_s, of a sphere of equivalent volume. While there is considerable uncertainty in the size estimates from field-ion microscopy (FIM) (7) and transmission electron microscopy (TEM) (8), the greater sampling statistics of small-angle neutron scattering (SANS) (9) give a well-defined size distribution defining an average particle size with 90% confidence limits comparable to the size of the squares plotted in Figure 3. Analysis of the SANS data incorporated the particle aspect ratio, β, determined from TEM of extracted particles, smoothly varying from near unity at initial nucleation to 4 at (near) equilibrium. The time dependence of average size suggests a smooth transition from nucleation to coarsening with suppressed growth characteristic of precipitation at high supersaturations as predicted by recent theories (10-12) based on the model of Langer and Schwartz (13). Nucleation in the ~0.1-0.5h regime is followed by a short growth regime between 0.5 and 1.0h, increasing average particle size from 36 to 56 Å. This is followed between 1 and 2h (bracketing the reaction half-time $t_{1/2}$ indicated by the volume fraction f_v curve) by a surprising second stage of nucleation which reduces the average particle size through an increased number of finer particles, bringing the total particle number density N_v (determined by SANS) to a maximum. This may represent an extreme form of a phenomenon encountered in the numerical modelling of precipitation at high supersaturation by Kampmann and Wagner (11) in which oscillations in nucleation rate are associated with crossovers between the average and critical particle sizes. Overall, the observations are consistent with the general features of high supersaturation behavior in which the major portion of solute depletion is associated with nucleation rather than growth, and the average particle size never differs greatly from the critical size. This constitutes a highly useful phenomenon for maintaining the finest possible particle size at completion of precipitation.

The volume fraction curve, determined from SANS, shows that precipitation is virtually complete after 10h tempering and very nearly complete after the standard 5 to 8h temper employed in practice. This is consistent with nearly complete dissolution of transient cementite for optimal toughness as emphasized by Speich (5,6).

TABLE 1

Alloy Steel Compositions (wt. pct.)

Commercial	C	Co	Ni	Mo	Cr	other
HY 180	0.11	8.0	10.2	1.0	2.0	0.18Mn
AF1410	0.16	14.25	10.15	1.05	2.10	--
Experimental						
1) 1410-4Mo	0.23	14.17	10.24	3.96	0.06	--
2) 1605-4Mo	0.24	15.99	4.96	4.03	0.02	--
3) 1605-MoCr	0.24	16.08	4.97	2.82	0.71	--
4) 1605-CrMo	0.24	16.06	4.98	1.52	1.40	--
5) 1605-4Mo(Nb)	0.24	16.02	4.97	4.03	0.02	0.029Nb
6) 1605-4Mo(NbV)	0.25	16.10	4.97	4.03	0.02	0.013Nb 0.006V
7) 1605-4Mo(Au)	0.23	15.92	5.03	4.10	0.02	0.07Au

Information on the state of interfacial coherency of the carbide particles can be deduced from the lattice parameters of extracted carbides measured by electron diffraction (8), also shown in Figure 3. In a coherent state the carbides will tend to reduce elastic energy by adopting a modified composition which reduces the overall magnitude of the orthorhombic lattice deformation relating the coherent HCP carbide to the BCC matrix. The smaller lattice parameters at shorter tempering times, observed here and in similar alloys (8), are consistent with such a reduction in the large positive BCC→HCP transformation strains in this system. The observed lattice parameter shifts suggest that the particles are coherent below 10 hr tempering and reach a fully incoherent state beyond 100 hr.

Measurement of the composition trajectories of the M_2C carbides presented in Figure 3 is made possible by the atom-probe field-ion microscope (APFIM) providing the necessary microanalytical resolution at the atomic scale (14-16); microanalysis of the coarser particles obtained beyond 10 hr tempering (17,18) is performed by scanning transmission electron microscopy (STEM). Compositions are represented as M_2C site fractions, with the bars at the right depicting the range of equilibrium compositions predicted by available thermodynamic databases (17). Although the carbide composition appears to ultimately reach equilibrium in the incoherent state, major departures from equilibrium exist at early stages of precipitation. Based on available data for the composition dependence of the M_2C lattice parameters (8), the depletion of C and enrichment in Fe are consistent with the observed lattice parameter shifts. In addition to elastic coherency effects, particle composition at small sizes will also be strongly influenced by capillarity. If the interfacial energy is not strongly composition dependent, the first particles will tend to adopt a composition corresponding to the maximum precipitation driving force; thermodynamic calculations of this composition suggest a reduced Cr/Mo ratio consistent with observation (19). The lattice parameter shifts and volume fraction measurements further suggest that the carbides achieve completion of precipitation in the coherent state, and are therefore close to a state of coherent equilibrium after 8 hr tempering of this steel.

The hardness curve in Figure 3 demonstrates that the completion of M_2C precipitation (and elimination of cementite) at 8-10 hrs tempering corresponds to an overaged condition. As mentioned earlier, strength in this regime is controlled by the Orowan bypass mechanism for which the strength achieved from a given volume fraction of precipitate can be increased by refining the particle size. Employing the information obtained from Figure 3, improved alloy compositions for more efficient strengthening can be sought from precipitation kinetic theory through control of appropriate scaling factors. In current theory of precipitation at high supersaturations (10-13), the principal scaling factors are (a) a diffusion time factor, which can be deduced from particle coarsening behavior, and (b) the initial critical nucleus size, inversely related to the precipitation thermodynamic driving force.

A rate constant for multicomponent particle coarsening, defining a diffusion time factor for multicomponent precipitation, has been derived by an extension (17,20) of the model of Bjorklund, Donaghey, and Hillert (21). The model has been tested (17, 20) by comparison of the relative $(Cr,Mo)_2C$ carbide coarsening rates in the experimental alloys 1 to 4 listed in Table 1. This series of alloys has a total Cr and Mo content balanced to 0.25 w/o C in the stoichiometry of the M_2C carbide, representing the minimum alloy content for complete replacement of cementite by M_2C. Alloy 1 (1410-4Mo) has the 14Co-10Ni matrix composition of AF1410, while alloys 2 through 4 (1605 series) have a 16Co-5Ni matrix which eliminates interference from austenite precipitation at long tempering times (17). Figure 4 plots the computed rate constant K defined in ref. 20, as well as the relative value (k/k_1) normalized to alloy 1. Despite the higher diffusivity of Cr relative to Mo and the lower thermodynamic stability of Cr_2C compared to Mo_2C, the model predicts a relatively low coarsening rate for the mixed $(Cr,Mo)_2C$ carbides (in part due to the stabilizing contribution of the entropy of mixing in the M_2C phase), as indicated in the lower curves for the 1605-.25C and 1410-.25C series. These stoichiometric compositions are predicted to have generally low coarsening rates (due to reduced Cr and Mo in matrix solution) as shown by comparison with the upper dashed curve representing 1410-.16 alloys with the lower carbon content of AF1410. Experimentally observed relative coarsening rates, k/k_1 as defined by the time dependence of average particle volume in 10 to 100 hrs tempering at 510C (17) are also plotted for alloys 1 to 4 and AF1410 in Figure 4. Apart from an anomalously high rate for alloy 2, the comparison supports the predicted lower coarsening rate of the stoichiometric alloys (by a factor of 20) compared to the non-stoichiometric AF1410, and supports the predicted multicomponent effects giving the mixed $(Cr,Mo)_2C$ carbides of alloys 3 and 4 coarsening rates comparable to the (more stable) Mo_2C carbide of alloy 1. These data must be viewed with some caution, however, as the alloys experienced some degree of decarburization during heat treatment. Overall, the coarsening model appears reasonable and could be applied to design of alloys with lower coarsening rates for thermal softening resistance (as in tool steels); in structural steels for room temperature applications it is more desirable to enhance the diffusional rate factor to accelerate secondary hardening at lower tempering temperatures.

The most important scaling factor governing the size scale of the precipitate dispersion (as well as the rate of nucleation) is the initial critical nucleus size. This in turn scales directly with the precipitate interfacial energy, and inversely with the precipitation thermodynamic driving force. The alloy composition dependence of the latter can be predicted from solution thermodynamics as conveniently treated by available computer software such as the THERMOCALC thermochemical database and software system (22). In order to treat coherent precipitation, however, it is necessary to modify the solution thermodynamics to incorporate the effects of elastic energy. The composition dependence of the M_2C carbide coherency strains (as described by the BCC→HCP lattice deformation accompanying coherent precipitation) can be prescribed from the composition dependence of the carbide lattice parameters (8). Using a simple isotropic homogeneous spherical inclusion model, it has been shown that the coherency elastic energy (in the limit of small carbide volume fractions) can be expressed in a form compatible with the solution free-energy functions employed in the THERMOCALC system allowing a simple modification of the database to treat the thermodynamics of coherent precipitation (19,23). Newer elastic calculations for anisotropic inhomogeneous ellipsoidal inclusions (using observed aspect ratios as represented in Figure 3) have been further refined to incorporate the effects of the redistribution of matrix substitutional solutes in the stress field of the coherent particle (24). This has been performed by an extension to

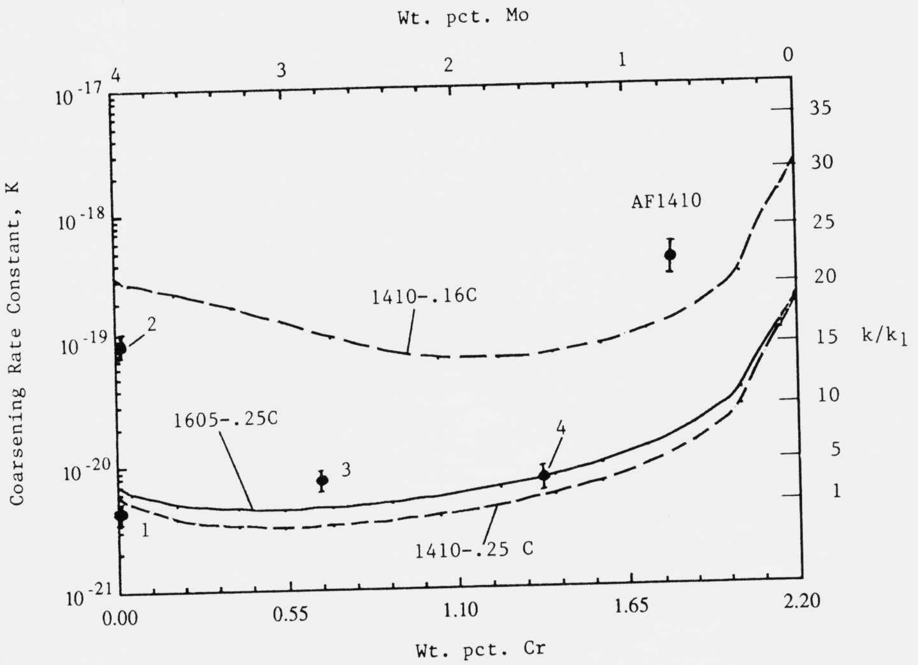

Fig. 4 Rate constants for $(Cr,Mo)_2C$ carbide coarsening in Ni-Co alloy steels with Cr and Mo contents stoichiometrically balanced to 0.24 w/o C.

multicomponent systems of the "open system" elastic constants method of Larché and Cahn (25) in which effective matrix elastic constants (incorporating solute redistribution) are defined from the solution chemical thermodynamics and the composition dependence of the matrix lattice parameters. Application to ferrite-M_2C coherent equilibrium in AF1410 is represented by Figure 5, depicting computed contours of constant hydrostatic stress and composition in the matrix surrounding a coherent M_2C carbide viewed along the matrix $[100]_\alpha$ direction corresponding to the habit direction of the rod-shaped particle (24). Dashed contours depict compressive stress and solute depletion, while solid contours represent tensile stress and solute enrichment. The predicted solute distribution (particularly for Ni and Co) should be measurable by high resolution microanalysis for the coherent particle size achieved after 8 hr tempering. Elastic energies computed from such linear elastic calculations represent an upper bound estimate. Assuming a composition-independent interfacial energy, reasonable agreement is obtained with measured M_2C composition trajectories in AF1410

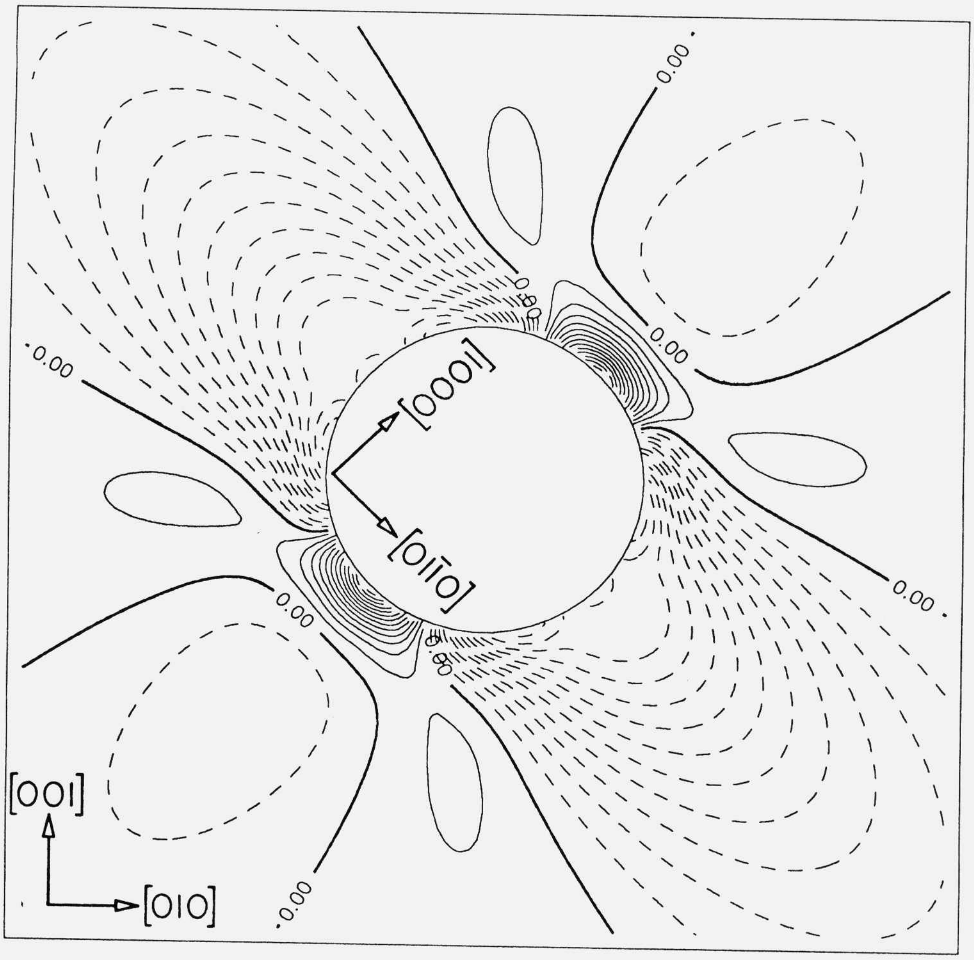

Fig. 5 Computed contours of constant hydrostatic stress and composition surrounding M_2C carbide in coherent equilibrium in AF1410 steel. Carbide viewed along $[100]_\alpha$ rod axis. Crystal axes of BCC α matrix and HCP M_2C carbide are indicated (24).

(Figure 3) and alloys 1-4 of Table 1 (17,18) when a correction factor of 0.25 is applied to the composition dependent elastic energy function defined by these calculations (26). This factor likely compensates for neglect of particle interaction with matrix dislocations to be discussed later.

A quantitative model for the thermodynamics of coherent M_2C precipitation allows prediction of alloy compositions capable of more efficient strengthening through refinement of the particle size. As mentioned in discussion of Figure 2, however, optimization of the metastable M_2C dispersion is constrained by kinetic phase competition with equilibrium phases such as M_6C and $M_{23}C_6$ which can precipitate incoherently on interfaces degrading toughness. This competition should also be amenable to control through alloy thermodynamics. Figure 6 shows a precipitation driving force map, constructed via THERMOCALC computations, showing contours of constant driving force (in kJ/mole) at 510C for precipitation of incoherent M_6C (Figure 6a) and coherent M_2C (Figure 6b) as a function of Cr and Mo content in alloys containing 14Co-10Ni-0.25C (26). The dashed straight lines represent stoichiometrically balanced compositions (as for the experimental alloys of Table 1) again corresponding to the minimum alloy content for complete elimination of cementite by M_2C precipitation. Intergranular embrittlement during 510C tempering of the experimental alloys (27), tentatively ascribed to M_6C precipitation, suggests a threshold driving force for M_6C nucleation under the tempering conditions of interest of 15 kJ/mole. The contour corresponding to this limit is superimposed as a dashed curve on the coherent M_2C driving force plot of Figure 6b. Through the competing influences of the chemical and mechanical thermodynamic contributions, the coherent M_2C driving force is nonmonotonic with Cr content, but increases with Mo. Maximization of the coherent M_2C driving force subject to the M_6C driving force constraint gives a unique optimum composition represented by the open point in Figure 6b. In parallel with these studies, an empirical alloy development program at Carpenter Steel (28) has arrived at a very similar composition demonstrating an excellent strength/toughness combination at a significantly higher strength than AF1410, supporting plausibility of the suggested thermodynamic design approach. It should be noted that the reference state for the driving force calculations of Figure 6 was fully supersaturated ferrite, while alloy carbide precipitation is in practice preceded by cementite precipitation which lowers the carbon potential. The effect can be estimated by adopting an initial state of ferrite-cementite paraequilibrium in which the cementite is constrained to inherit the substitutional composition of the alloy (29). The lower carbon potential reduces the M_6C driving force by ~0.7kJ/mole and the coherent M_2C driving force by ~2.7 kJ/mole with a slight distortion of the contour shapes of Figure 6 (26).

The influence of the high Co recovery-resistant matrix on M_2C secondary hardening behavior is shown in Figure 7 comparing 1 hr isochronal tempering hardness curves for a simple 4Mo-.23C steel (30) and for alloy 1 of Table 1, with the same Mo and C content but containing 14Co-10Ni (17). In

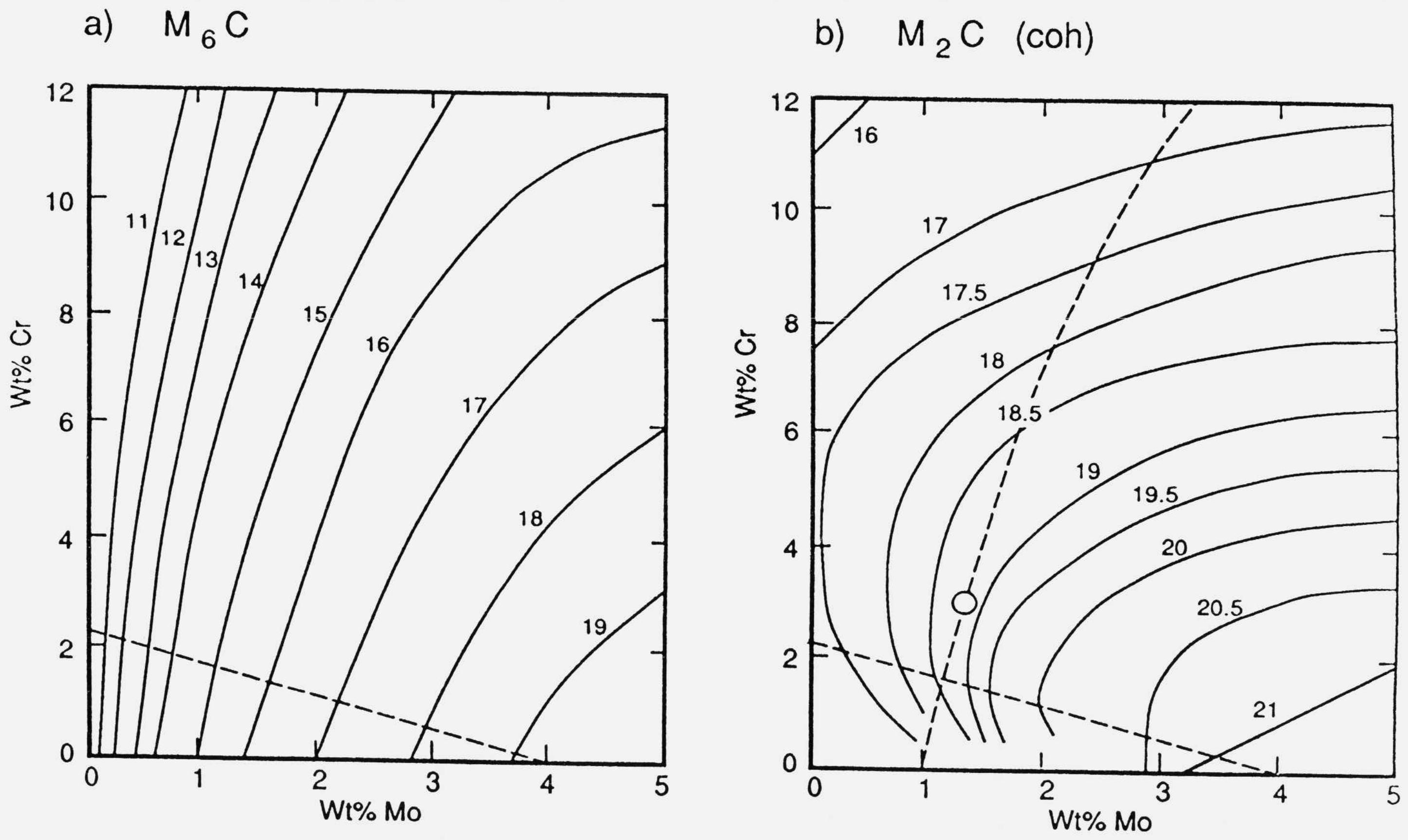

Fig. 6 Computed precipitation driving force (kJ/mole) at 510C for alloys containing 14Co-10Ni-0.25C: (a) incoherent M_6C, (b) coherent M_6C (26).

the latter steel the secondary hardening peak temperature is moved down 100°C with a $10R_c$ point increase in peak hardness. Comparison of the isothermal hardening behaviors at 500°C (31,32) shows an acceleration of secondary hardening in the Co-Ni steel by 2 to 3 orders of magnitude. Such a strong acceleration allowing a substantial reduction in secondary hardening temperature (with an attendant increase in precipitation driving force) is consistent with a switch to heterogeneous nucleation on dislocations in the recovery-resistant Co-Ni steels as proposed by Speich (5,6).

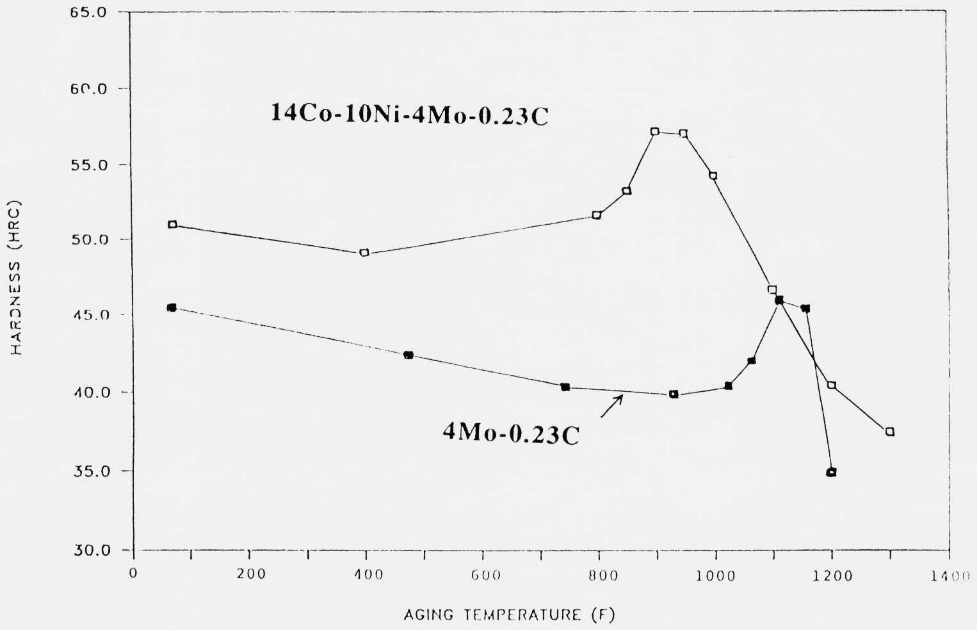

Fig. 7 Isochronal tempering hardness curves (1 hr) for 4Mo-0.23C steels with and without 14Co-10Ni.

The observed acceleration and enhancement of secondary hardening is similar to the nucleation effects of small additions of MC carbide formers (e.g. Nb,V) and GP-zone formers (e.g. Au) to simple Mo-C steels studied by Honeycombe and coworkers (31,33). To investigate the possibility of superimposing the two types of nucleation phenomena, the effect of Nb, V, and Au additions on the secondary hardening response of the Co-Ni alloy 2 of Table 1 was studied in the series of alloys represented by alloys 5 to 7 (15). Observed hardening enhancement was limited to the level of ~1 R_c point, and extensive atom-probe microanalysis indicated preferential acceleration of M_2C nucleation by the high dislocation density such that there was little interaction with either MC precipitation or GP zone formation which required a longer time scale. Although some Au clustering was observed both in the matrix and M_2C suggestive of some degree of M_2C nucleation on Au zones, the Nb and V were found only in the M_2C phase with no indication of separate MC formation in near-peak-hardness microstructures. The measured compositions of M_2C carbides in alloys 5 to 7 are listed in Table 2. Following this demonstration of Nb and V solubility in M_2C, subsequent coherent thermodynamic calculations have indicated that V can be a very effective alloy addition to enhance the precipitation driving force for coherent M_2C (26).

TABLE 2

M_2C Compositions in Trace-Addition Alloys
(510°C/100hr temper)

Alloy		Carbide Formula
#5)	1605-4Mo (Nb)	$(Mo_{0.94\pm0.04}Fe_{0.04\pm0.01}Nb_{0.02\pm0.01})_2C_{0.88\pm0.02}$
#6)	1605-4Mo(NbV)	$(Mo_{0.95\pm0.04}Fe_{0.03\pm0.01}Nb_{0.01\pm0.01}V_{0.01\pm0.01})_2C_{0.92\pm0.03}$
#7)	1605-4Mo(Au)	$(Mo_{0.98\pm0.03}Fe_{0.018\pm0.01}Au_{0.002\pm0.001})_2C_{0.90\pm0.02}$

The strong effect of heterogeneous nucleation at dislocations on the M_2C carbide precipitation behavior emphasizes the important role of Co in retarding dislocation recovery so that a high dislocation density can be retained at secondary hardening temperatures. Neutron diffraction has revealed the presence of short-range order (SRO) in precipitation-hardening high Co martensitic steels (34), and field-ion microscopy has indicated SRO in AF1410 (35). Based on the hypothesis that the recovery resistance is associated with SRO, recovery behavior has been investigated by TEM (36) in the simple ferritic binary Fe-Co and Fe-Al alloy systems where previous studies have demonstrated SRO by neutron diffraction (37) and TEM (38), respectively. The recovery behavior in the temperature range of 400 to 600C was also compared with that of Fe-Ni and Fe-Ni-Co martensitic alloys (36). Figure 8 shows the retarded softening behavior at 527C for cold-worked Fe-14Co and Fe-6Al compared to Fe as expressed by the hardness decrease ΔH relative to the decrease for full recrystallization ΔH_{REX}. As indicated in the figure, a preliminary neutron diffraction measurement (39) confirmed the existence of SRO in the Fe-14Co alloy after 1 hr at 527C. The heavily cold-worked initial structure of these alloys showed a deformation microband substructure very similar in character and size scale (~0.25 µm width) to the lath structure of the martensitic alloys, and showed similar stages of recovery consisting of (a) reduced general dislocation density, (b) sharpening of dislocation walls, and (c) polygonization and subgrain coarsening. The measured parabolic rate constant for subgrain coarsening at 527C showed an order of magnitude reduction for Fe-14Co (2.2 x 10^{-7} $\mu m^2/s$) compared to Fe (2.8 x $10^{-6} \mu m^2/s$). While the Fe-Ni martensites showed monotonic softening behavior, the Fe-Ni-Co martensites showed hardening similar to previous observations interpreted as SRO strengthening (40). After full recrystallization at 800 to 830C, the ferritic Fe-Co and Fe-Al alloys also showed some hardening with aging at 420 to 575C. Although some preliminary Mossbauer spectroscopy on the Fe-Co and X-ray diffractometry on the Fe-Al did not yield supporting evidence for SRO (36), the bulk of the literature observations (34,37,38) and the neutron diffraction evidence (39) suggest that SRO is the most plausible basis for both the hardening and recovery resistance. In addition to increased dislocation glide resistance indicated by the observed hardening, dislocation climb processes important to recovery may be inhibited through a reduction of diffusivity by SRO as has been demonstrated in Cu-Zn (41). A more quantitative understanding of the mechanism of recovery resistance could allow both the more effective use of Co and some degree of substitution of other ordering elements such as Al in secondary hardening steels.

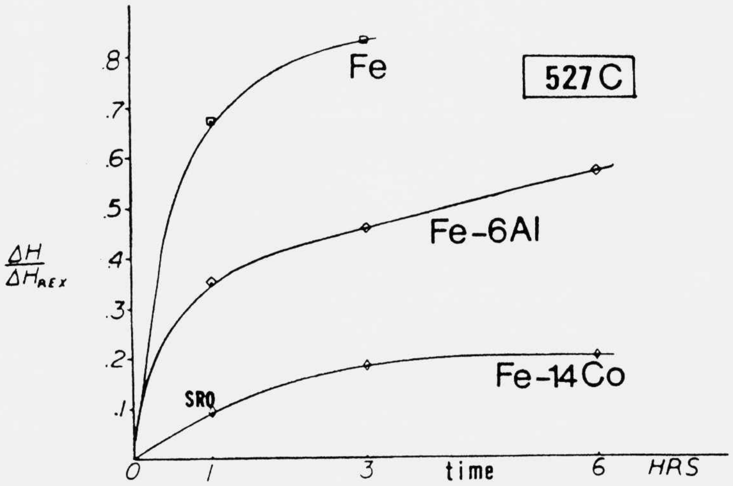

Fig. 8 Relative hardness decrease ΔH, normalized to full hardness decrease with recrytallization ΔH_{REX}, during 527C isothermal recovery of heavily cold-worked ferritic Fe, Fe-6Al, and Fe-14Co, showing retarded softening with alloying (36).

A longer-range issue regarding the achievement of maximum carbide strengthening for a given alloy carbon content concerns the properties of the carbide phase itself. In overaged structures characteristic of the completion of precipitation, size refinement will increase strength until a critical size is reached below which strength is controlled by particle shearing rather than the Orowan bypass mechanism. As discussed by Hornbogen (42) the critical particle size for this transition, and alloy strength in this regime, is controlled by the mechanical behavior of the dispersed phase; the high elastic modulus of alloy carbides compared to intermetallic phases makes them efficient obstacles capable of Orowan strengthening at smaller particle sizes. The ultimate design of optimal carbide strengthening dispersions will require information on the mechanical properties of the M_2C phase which can be obtained by synthesis of the multicomponent M_2C carbides of interest in bulk form. Such an investigation is currently underway (43).

TOUGHENING AND SHEAR LOCALIZATION

The role of primary void formation at inclusion particles in ductile fracture is well established. Major improvements in the fracture toughness of high-strength steels in the past two decades have accompanied improved processing technology providing "clean" steels with reduced inclusion volume fractions; more recent work has demonstrated the importance of inclusion spacing in ductile fracture (44). Less well understood is the role of finer ~0.1μm scale secondary particle dispersions which nucleate microvoids promoting shear localization, accelerating the process of primary void coalescence (45). In clean steels, the shear localization can dominate ductile fracture causing a mode I-loaded crack to locally adopt a mixed mode I and II "zig-zag" form of crack propagation. In addition to its microscopic role in mode I fracture toughness, shear localization also represents an important macroscopic failure mode limiting ballistic performance of ultrahigh-strength steels in armor and ballistically-tolerant structural applications (46). Not only are the structure/property relations governing shear localization currently poorly defined, but due to experimental difficulties associated with the finer particle size relative to the well-studied ~1 μm-scale primary inclusions, the microvoid nucleating particle dispersions are generally poorly characterized, constituting one of the least controlled components of steel microstructures. Control of shear localization represents the current frontier in the enhancement of ductile fracture resistance of ultrahigh-strength steels. As depicted in Figure 2, efforts to control shear localization behavior focus on (a) the role of secondary particle dispersions (primarily grain refining dispersions) in microvoid nucleation and associated softening, and (b) the role of matrix constitutive behavior, as most effectively controlled through application of transformation plasticity provided by finely dispersed metastable austenite.

Shear Instability and Particle Dispersions

Shear localization behavior in ultrahigh-strength martensitic steels has been effectively investigated using shear tests conducted with and without compressive loading superimposed normal to the shear plane (47-49). Not only do the shear test specimen geometries allow relatively large amounts of material to be uniformly deformed to the point of shear instability, but the operating stress states provide no driving force for primary void growth, forcing the materials to fail entirely by the macroscopic shear localization mode. The experiments thus selectively study behavior associated with the microstructural component of interest: the microvoid nucleating particle dispersions. Tests are conducted using both thin-wall torsion and a linear-shear geometry allowing superimposed compressive loading. The critical shear instability strain, γ_i, is measured as the imposed uniform strain beyond which deformation localizes in shear bands, and corresponds to a maximum stress in the shear stress-strain (τ-γ) curve. The γ_i values measured in an air-melted 4340 steel with and without an applied normal compressive stress of 1/3 σ_y are plotted versus R_c hardness level in Figure 9 (47,48). Hardness is varied by 1-hr tempering at temperatures corresponding to Stage I (ε-carbide strengthening, R_c56), Stage II (retained austenite decomposition, R_c 49-51), and Stage III (Θ-cementite strengthening, R_c 30-40) tempering. The instability strain generally decreases with increasing hardness level with an anomalous dip in Stage II tempering corresponding to "tempered-martensite embrittlement" associated with interlath cementite precipitation via austenite decomposition. The large increase in γ_i with compressive stress is consistent with a pressure-sensitive microvoid softening mechanism of shear instability. The role of microvoid formation in driving the instability is supported by TEM and SEM observations of microvoids in material deformation just to γ_i (47,58) but such observations of fine voids associated with ~0.1 μm scale particles are not easily reproduced. Some preliminary experiments performed on the same material suggest that small-angle X-ray scattering measurements may allow detection of early stage microvoid formation in thin sections of deformed shear-test specimen gage sections (50).

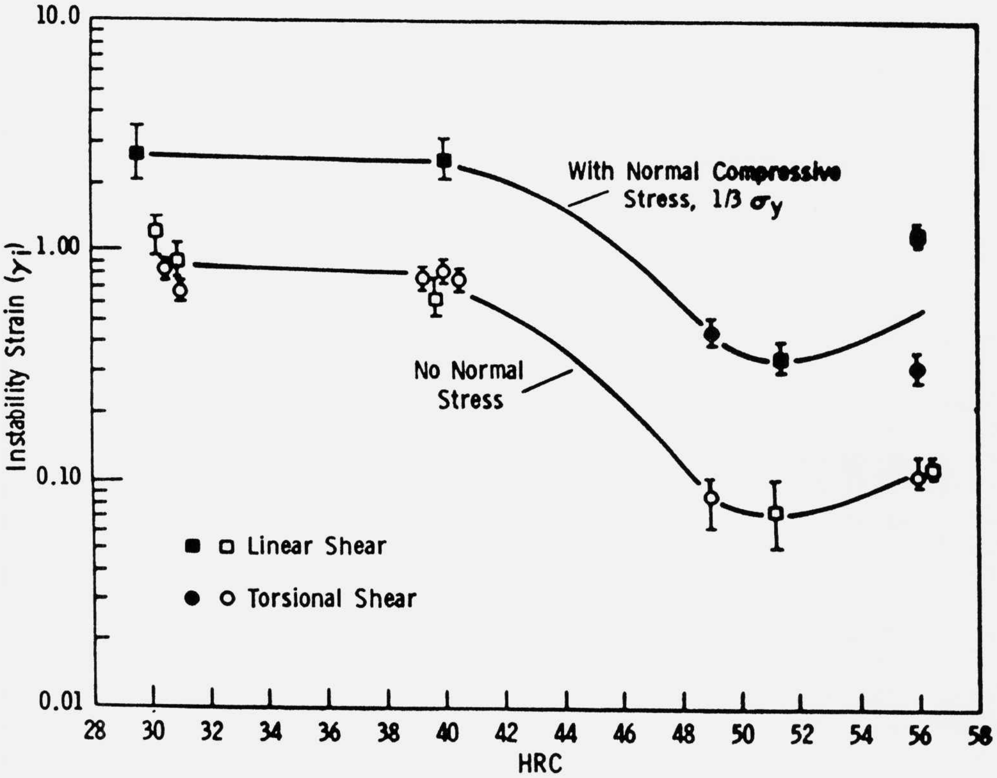

Fig. 9 Measured shear instability strain γ_i for 4340 steel as a function of hardness with and without normal compressive stress of 1/3 σ_y (48).

Comparison of the instability strain measured in high-hardness 4340 under isothermal conditions at a strain rate of $10^{-3}s^{-1}$ and under adiabatic conditions at $10^{2}s^{-1}$ gives the surprising result that γ_i is unchanged (47,48). While thermal softening under adiabatic deformation conditions may well contribute to shear localization in the highly compressive stress states associated with ballistic performance (46), it does not appear to significantly contribute to localization under pure shear stress. This would presumably also apply in tensile stress states such that improved resistance to microvoid formation should improve localization-controlled fracture toughness in ultrahigh-strength steels under both quasistatic and dynamic conditions.

An abrupt nature of shear localization observed in steels at ultrahigh strength levels together with the small degrees of microvoiding observed just prior to its onset implies that the microvoid softening is nucleation controlled rather than growth controlled at these strength levels. A crucial tool for the theoretical investigation of structure/property relations governing microvoid nucleation and its associated softening has been the finite-element cohesive zone void nucleation model of Needleman (51,52). Prescribing a local force-distance law for interfacial separation defining a characteristic length scale, the complete process of interfacial decohesion of a rigid spherical particle in an isotropically hardening elastic viscoplastic matrix is modelled as a function of particle diameter, d, particle volume fraction, f, and interfacial cohesive characteristics (separation work $\Delta\gamma$ and interaction range δ). The predicted nature of nucleation is depicted in Figure 10 showing a quadrant of a cell with a particle centered at its lower left corner; equivalent strain contours in the matrix and interfacial configurations during separation are depicted for four applied remote strain levels $\varepsilon_1<\varepsilon_2<\varepsilon_3<\varepsilon_4$ in axisymmetric tensile deformation. Abrupt decohesion at the top of the particle is followed by spreading along the interface. The macroscopic stress-strain response associated with these processes in a material with a periodic array of such cells is summarized in Figure 11 comparing materials with three particle sizes $d_1<d_2<d_3$. The upper dashed curve represents the rigidly bonded case while the lower dashed curves correspond to replacement of the particles with voids of the same volume fraction, f. The largest particle size (d_3) shows the earliest nucleation with severe (brittle) softening behavior. Reduced particle size not only delays nucleation, but reduces softening via a more gradual (ductile) process of interfacial decohesion. Identical effects are observed by reducing f at fixed d. Fitting the model to measured microvoid nucleation conditions in steels for which d and f data are available allows an estimate of interfacial cohesive properties (52), with which the model can then predict quantitative benefits of variations in d and f. Stress states of the shear test experiments have been simulated by superimposing hydrostatic compressive stress, while retaining the axisymmetric deformation approximation (53).

Analytical modelling by Hutchinson and Tvergaard (54,55) has elucidated both the nature of void/particle interactions promoting void growth in shear deformation, and the strong strain softening influence of void nucleation. Matrix plastic flow associated with load shedding from the decohering interface is shown to give stronger strain softening than had previously been expected. Further analyses (56) have gone beyond isolated particle and periodic cell models to explore the influence of nonuniformity of particle spatial distributions, demonstrating the manner in which clustering can further accelerate nucleation. As the basis of a more detailed accounting of the directional

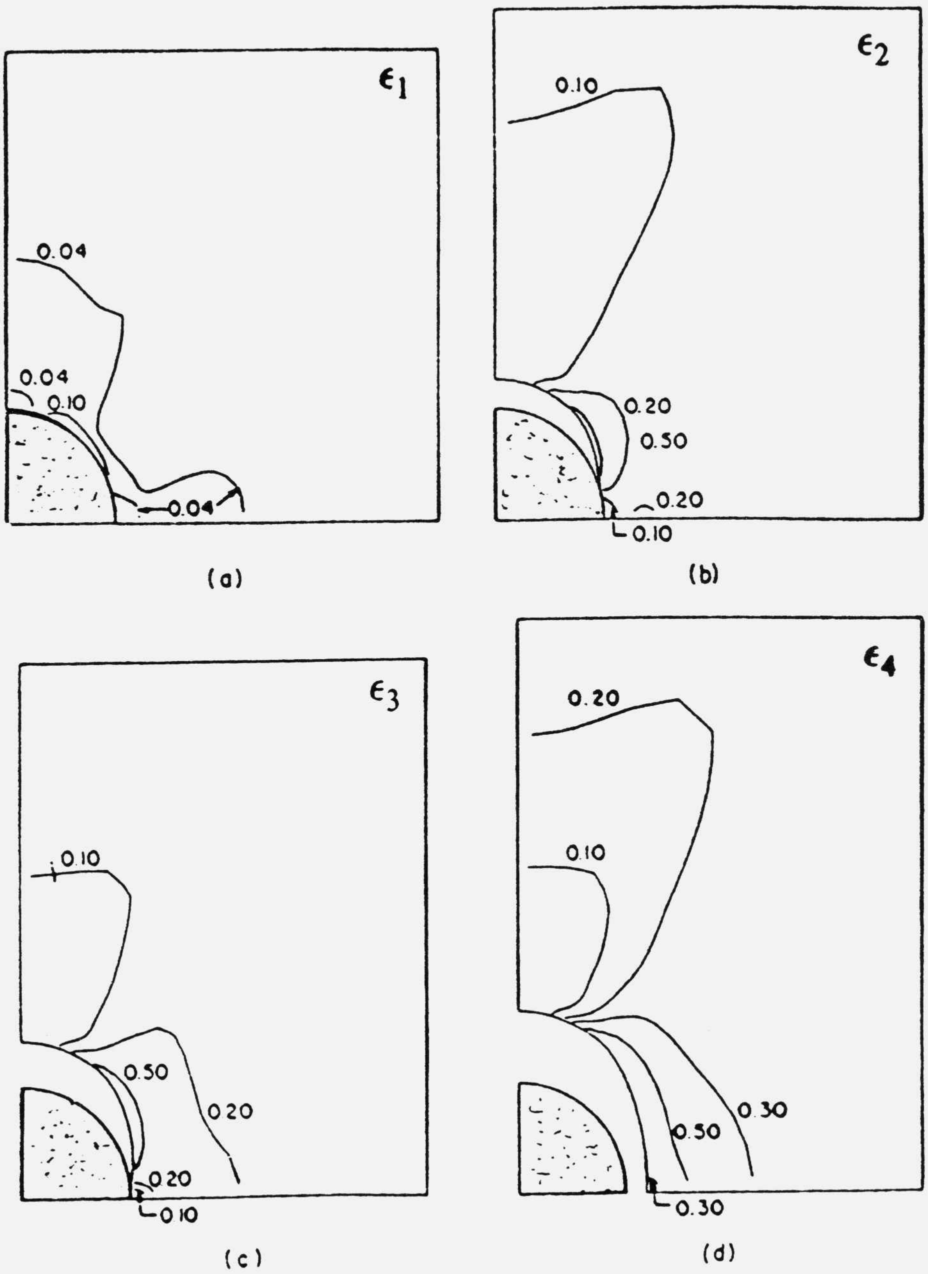

Fig. 10 Quadrant of cell model showing matrix strain contours and interface geometry during particle interfacial debonding at increasing applied strain levels (51).

particle pair interactions underlying local cluster behavior, Tracey and Perrone (57,58) have performed three-dimensional finite-element calculations of the deformation fields between pairs of spherical voids and particles in a plastic matrix undergoing the plane-strain shear deformation imposed in the shear test experiments, adopting constitutive relations appropriate to carbide particles in high hardness 4340 steel. Pairs of voids lying in the shear plane are found to exhibit the strongest interaction in a direction normal to the shear direction, while particle pairs exhibit strongest interaction when aligned parallel to the shear direction. Such analyses should ultimately allow control of anisotropic shear localization behavior in wrought alloys with anisotropic particle distributions.

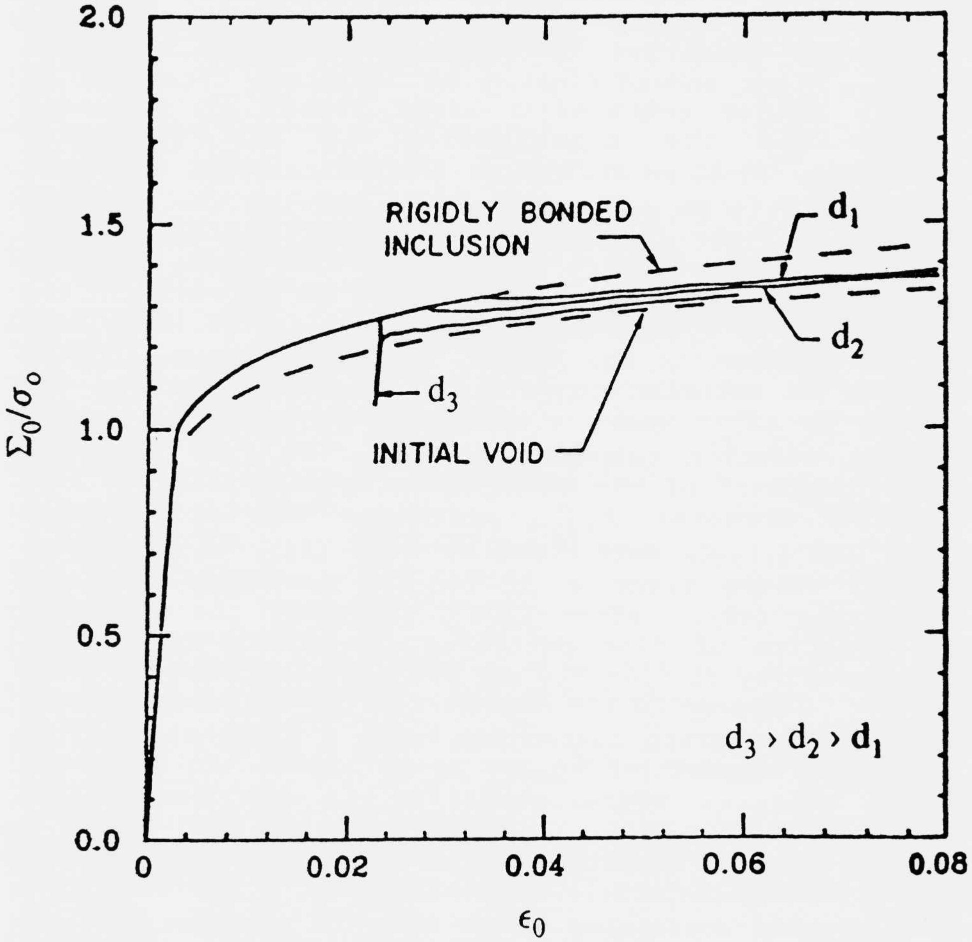

Fig. 11 Computed macroscopic stress-strain response during void nucleation at different size particles (51).

To experimentally examine the influence of particle dispersion variations on shear localization behavior, the same shear tests performed on the air-melted (AM) 4340 of Figure 9 have been extended to 4340 steels processed by vacuum-arc remelting (VAR) and rapid solidification processing (RSP) by centrifugal atomization and hot consolidation (48,49,59) and the particle dispersions quantitatively characterized by TEM and STEM analysis of thin foils and extraction replicas (49,59,60). In the stage III tempered condition, shear localization is found to be dominated by the cementite dispersion precipitated on tempering and is relatively insensitive to earlier stages of processing. In contrast, the much finer ε-carbide strengthening dispersion precipitated in Stage I tempering does not participate in microvoid nucleation, and shear localization is controlled by the grain refining particle dispersion which remains undissolved during austenitizing, and which is sensitive to solution treatment and melt practice. After conventional 1 hr. solution treatment at 840C, the AM4340 contains a large number of 50nm AlN particles and the distribution of MnS particles (predominantly 10-20 μm stringers) includes a small component of spherical 0.16 μm particles (60). Raising the solution temperature to 1100C dissolves the small sulfides and reduces the apparent number density of AlN particles by an order of magnitude (60). This is accompanied by an increase in the shear instability strain at R_c55 hardness from ~0.15 to 0.23 (47). In contrast to the AM4340, a more detailed study of the effect of solution temperature on the VAR4340 in the range 870 to 1200C shows a monotonic decrease of γ_i with increasing solution temperature (49). In this case the dominant component of the grain refining dispersion at 870C is 0.17μm diameter $M_{23}C_6$ carbides of composition $(Fe_{.74}Cr_{.25}Mo_{.01})_{23}C_6$ determined by STEM (60), with a total dispersion volume fraction of f=0.44% estimated from SEM metallography (49). After 1200°C treatment the estimated volume fraction of fine particles is reduced to f=.05%, consisting mainly of 80nm Ti(C,N) and a small amount of 50 nm Al_2O_3 (49). Compared to the AM4340, the VAR4340 shows greater high temperature grain coarsening, with a grain diameter of 17 μm at 870C coarsening to 280 μm at 1200C. In Stage III tempered material where cementite is the predominant microvoid nucleation site, γ_i decreases by the same factor on increasing solution temperature from 870C to 1200C as for the Stage I tempered material, suggesting the γ_i decrease is a feature of grain coarsening rather than the changing particle distribution. The RSP 4340 exhibits a highly stable grain refining dispersion of 0.27 mm Al_2O_3 with f=.26%; the dispersion, grain size, and γ_i are not significantly changed on increasing the solution temperature from 870 to 1200C (49).

Comparison of shear tests, slow-bend Charpy tests, and K_{IC} tests in the Stage I tempered (R_c53) VAR4340 (49) revealed a correlation between γ_i and Charpy energy consistent with the demonstration by metallographic sectioning of bend specimens that failure in the blunt notch initiates by shear localization for both coarse and fine grained microstructures. Sectioning of K_{IC} specimens loaded to 90% K_{IC} showed that sharp crack propagation in the fine grained 870C treated material occurs by "zig-zag" shear localization with a 10μm wavelength, while an anomalous increase in K_{IC} in the 1200C-treated coarse-grained material is associated with intergranular microcracking which increases the fracture process zone by more than an order of magnitude. This peculiar effect of grain coarsening does not appear to represent a practical toughening mechanism in view of the associated degradation in shear localization resistance revealed in other test geometries. Accelerated shear localization in the coarse structures may be related to texture softening effects associated with crystal slip behavior (61).

Comparative shear, Charpy, and K_{IC} testing of fine-grained VAR processed AF1410 steel shows strong correlations indicative of a dominant role of microvoid nucleation and shear localization in all three geometries. With a standard 830C solution treatment, comparison of underaged and overaged materials of the same hardness shows the accelerated microvoid nucleation effect of undissolved cementite in the underaged material as revealed in a reduction of both γ_i and K_{IC}. The results indicate a direct scaling between γ_i and the critical crack opening displacement (COD) for propagation (47). In the standard 510C 5h tempered condition (slightly overaged), a modest increase in solution temperature from 830C to 885C is found to produce a significant improvement in strength/Charpy toughness combination without excessive grain coarsening (62). Examination of the particle dispersions present at these two temperatures demonstrates that the temperature increase greatly simplifies the dispersion from a list of 6 phases to a single (Ti,Mo)(C,N) phase as summarized in Table 3 (49). Although the strength is slightly reduced by the higher solution treatment, a lower temperature post-age treatment for enhanced Co ordering is found to restore a normal strength level while maintaining a 40% enhancement in Charpy toughness (49, 62). These experiments demonstrate how, for a fixed melt practice, fine-tuning of solution treatment to eliminate unnecessary particles can provide an optimal grain refining dispersion maintaining a sufficiently fine grain size while enhancing toughness through improved microvoid nucleation resistance.

TABLE 3

Particles in AF1410

Solution Temp.		Particle Type	Size Range
1525°F	(830°C)	$(Ti,Mo)_xC,N$	10 - 180 nm
		$(Cr,Fe,Mo)_{23}C_6$	50 - 125 nm
		$(Fe,Cr,Mo)_{23}C_6$	75 - 105 nm
		$(Mo,Cr)_xC$	30 - 65 nm
		$(Mo,Fe)_xC$	40 - 50 nm
		Mo_xC	5 - 10 nm
1625°F	(885°C)	$(Ti,Mo)_xC,N$	20 - 35 nm

Information on interfacial cohesion for phase selection for grain refining dispersions can be derived from nucleation experiments on well characterized microstructures. Interpreting the measured shear localization strains as microvoid nucleation strains in the fine-grained 870C-treated VAR4340 and RSP4340, a fit of the Needleman numerical nucleation model using the measured $\bar{d}$ and f for the $M_{23}C_6$ and Al_2O_3 dispersions has provided an estimate of the interfacial strength (or work of separation) indicating superior interfacial cohesion for $M_{23}C_6$ compared to Al_2O_3 (53). The intrinsic work of interfacial separation per unit area, $\Delta\gamma$, can be expressed by:

$$\Delta\gamma = \gamma_P + \gamma_M - \gamma_{IPB}$$

where γ_P and γ_M are the particle and matrix free surface energies and γ_{IPB} is the particle/matrix interphase boundary energy. While γ_{IPB} is difficult to anticipate, phases with high cohesive energy (which also promotes high stability and coarsening resistance to maintain fine dispersions) will tend to have higher free surface energy γ_P promoting higher $\Delta\gamma$. Such simple considerations imply Al_2O_3 should be superior to $M_{23}C_6$, contrary to experiment. In practice, interfacial cohesion will likely be strongly influenced by impurity segregation through mechanisms to be addressed in our discussion of grain boundary cohesion. High resolution microanalysis of these interfaces will likely play an important role in the full characterization of the structural basis of microvoid nucleation resistance. In the meantime, quantitative estimates allowed by currently available nucleation experimental data indicate that TiC possesses the highest interfacial cohesion in steels (63). The observation of the closely related (Ti,Mo)(C,N) phase in an optimally solution-treated (Table 3) commercial AF1410 composition which is the product of an empirically optimized melt practice, further supports the merit of this compound for intrinsic nucleation resistance. Experiments to quantify the interfacial cohesion of this phase in AF1410 are underway (64).

While nucleation models can prescribe the dependence of microvoid nucleation resistance on average particle size, $\bar{d}$, and volume fraction, f, optimization of a grain refining dispersion requires a description of the dependence of grain refinement on these same variables. Based on an extensive quantitative study of grain refinement in VAR and RSP matrix tool steels, Hsu (65) has synthesized boundary pinning models of Gladman (66) and Hellman-Hillert (67) to define the average grain diameter D stabilized by the boundary pinning interaction of a dispersion of stable (static) particles of distributed size:

$$\bar{D} = \frac{4}{3\alpha}\left(\frac{3}{2} - \frac{2}{Z}\right)\left(\Sigma\frac{f_i}{d_i}\right)^{-1} .$$

Here, f_i is the volume fraction of particles of diameter d_i, Z is a grain size distribution parameter defined by the ratio of the largest grain to the average grain size, and α represents the range of boundary/particle interaction normalized to the particle size. In the approximation of monodispersed particles of diameter, $\bar{d}$, and total volume fraction, f, the expression simplifies to:

$$\bar{D} = \frac{4}{3\alpha}\left(\frac{3}{2} - \frac{2}{Z}\right)\frac{\bar{d}}{f} .$$

Figure 12 summarizes the observed correlation (with $\alpha = 1$) between D and $(\Sigma f_i/d_i)^{-1}$ for VAR and RSP processed M-2 and M-50 matrix tool steels over a wide range of solution temperatures, and includes available literature data (68-70) relating D and $\bar{d}/f$ in other steels. The beneficial grain refining effect of fine particle sizes in hot-consolidated RSP material is partly offset by a broader grain size distribution represented by a higher Z. The ability of RSP processing to disperse highly stable, coarsening resistant compounds such as oxides and oxysulfides on a fine size scale for efficient boundary pinning has allowed achievement of remarkable high temperature grain coarsening resistance in a wide range of steels (71); the phenomenon offers the potential for practical exploitation of high solution treatment temperatures in the high toughness secondary hardening steels of concern here.

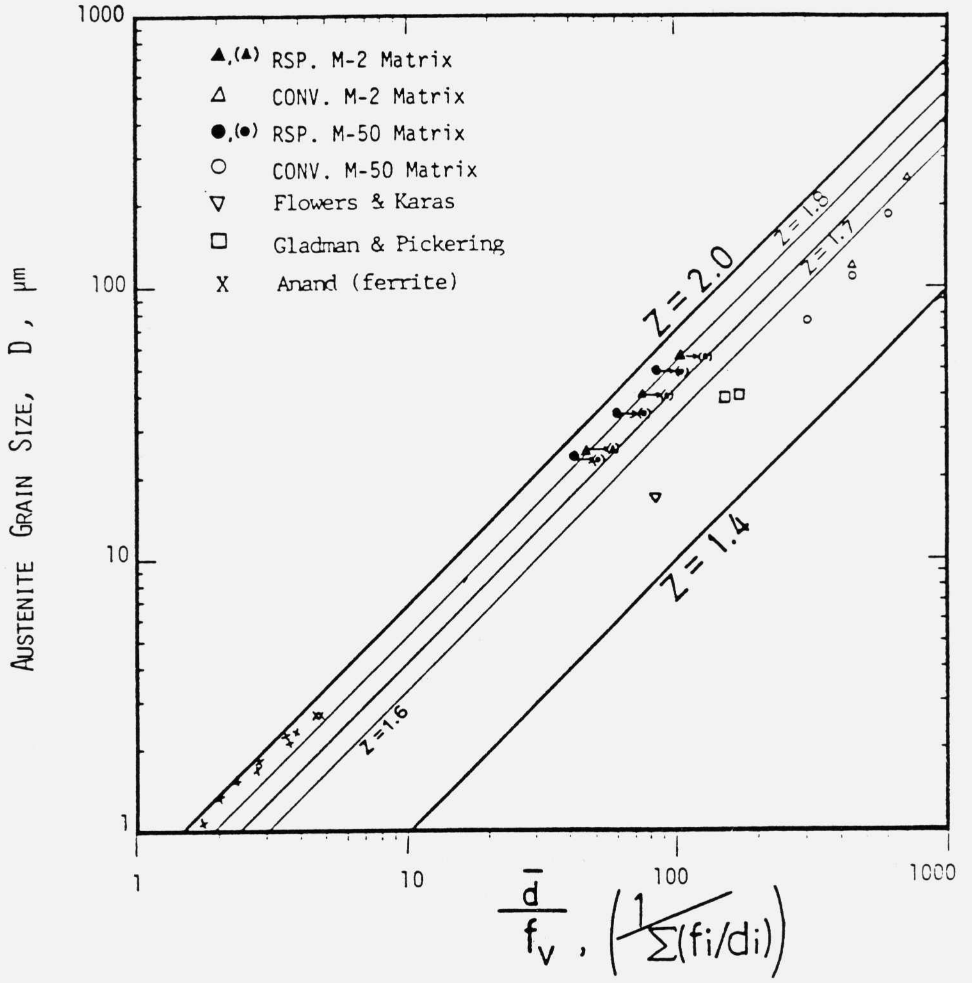

Fig. 12 Comparison of grain size data for steels with average particle size and volume fraction. Arrows show shift associated with summation over particle size distribution. Straight lines depict model predictions for various values of grain size distribution parameter, Z (65).

Since maintaining a desired grain size requires a fixed ratio of d to f, and nucleation resistance (as in Figure 11) depends monotonically on both variables, geometric optimization of the grain refining dispersion then requires minimization of both d and f at fixed d/f. However, it can be anticipated that at sufficiently small particle size the Gladman type of static particle/boundary interaction just discussed will no longer apply as thermally activated boundary unpinning reduces the net interaction force exerted by the particles. Modelling such unpinning behavior by an adaptation of thermally activated deformation theory gives the effective pinning behavior described in Figure 13 (72). Figure 13a depicts the required f to maintain a 10μm grain size in a steel after 1 hr at 870C and 1200C as a function of particle size d. The straight line corresponds to the Gladman-type static interaction. Below a critical particle size, higher f is required for boundary pinning to compensate the effect of thermal activation. Adopting the f-d curve for 1200C solution treatment as inputs to the Needleman nucleation model, preliminary calculations of microvoid nucleation strain vs. particle size (with f constrained to maintain constant D) for R_c53 VAR 4340 with an $M_{23}C_6$ dispersion give the behavior depicted in Figure 13b (53). Although thermal activation ultimately limits improvements achievable at very small particle sizes, the model predicts that modest size refinement below the current level of d = 0.17μm can yield substantial improvement in microvoid nucleation resistance. Maintaining the desired finer particle sizes during solution treatment will require more stable coarsening resistant phases such as those accessible through rapid solidification processing.

While experiments have already demonstrated substantial toughness enhancement in AF1410 through improved solution treatment to eliminate unnecessary dispersed particles, evolving theoretical guidelines and preliminary quantitative estimates indicate that even greater improvements in microvoid nucleation resistance await the design of optimal grain refining dispersions via combined phase selection and process control to achieve prescribable dispersion geometries.

Transformation Toughening

As emphasized by Krauss (45), equally important to shear localization as the role of particle dispersions is the role of the constitutive behavior of the matrix in which the particles reside. The most dramatic means of altering matrix constitutive behavior to delay shear localization and ductile fracture is the transformation plasticity that can be obtained from a dispersion of metastable austenite, as also represented in Figure 2. Transformation plasticity resulting

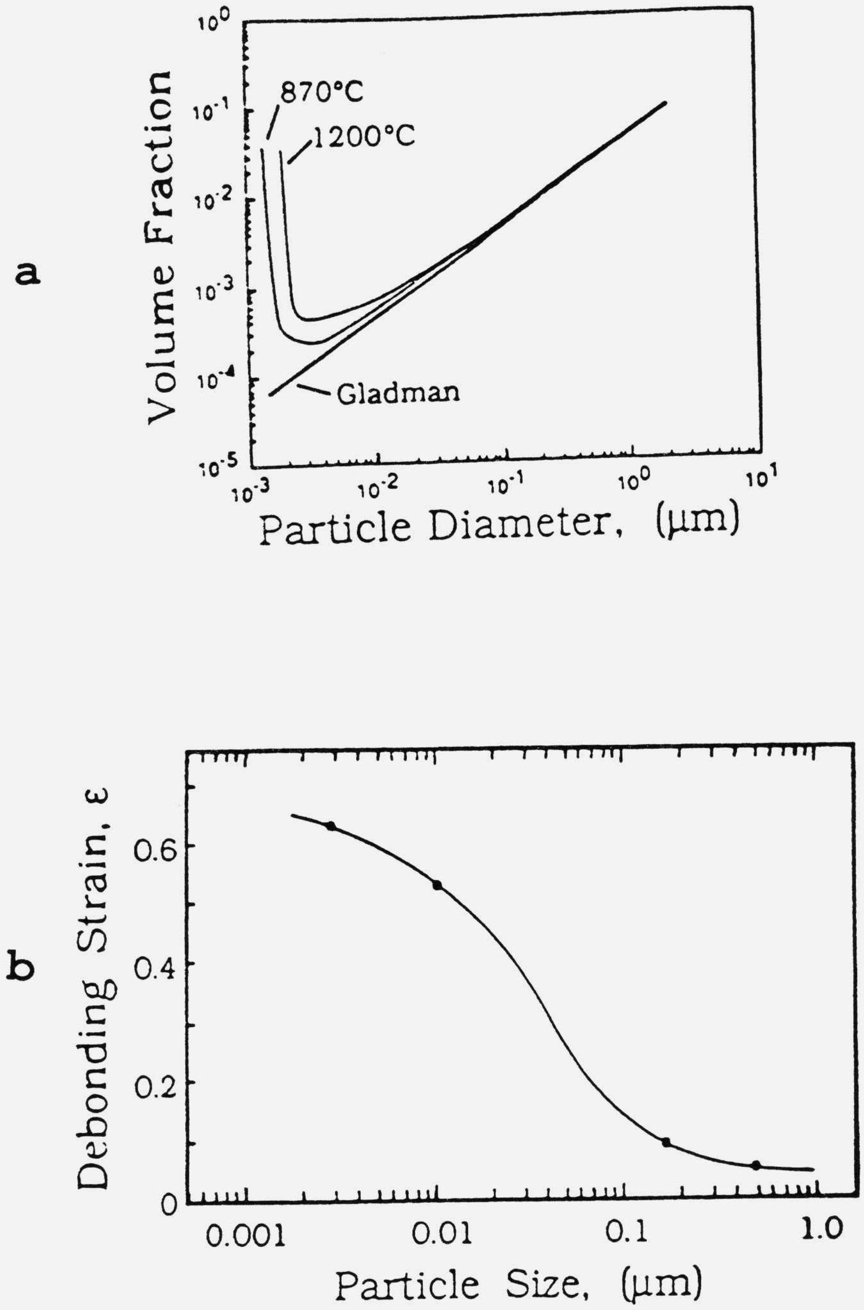

Fig. 13 Void nucleation on grain refining dispersion. (a) Necessary particle volume fraction vs. particle diameter to maintain 10μm grain size after 1 hr at 870C and 1200C accounting for thermal activation, (b) Particle debonding strain vs. particle diameter employing volume fractions of (a) in Needleman model.

from martensitic transformation during deformation has been most thoroughly investigated in fully austenitic steels (73), identifying two basic modes of transformation. Stress-assisted transformation involves the same nucleation sites as the spontaneous transformation on cooling, but assisted by the thermodynamic effect of applied stress, while strain-induced transformation is controlled by the production of new nucleation sites by plastic deformation. Different transformation product morphologies tend to be associated with these two modes: stress-assisted transformation giving relatively coarse plates, while the strain-induced transformation develops as fine laths typically formed at intersections of shear microbands. Kinetic models and quantitative constitutive relations for associated transformation plasticity have been developed for both the stress-assisted (74) and strain-induced (75,76) modes. Both modes promote sigmoidal stress-strain (σ–ε) curves with an initial upward curvature deriving from the combined influence of a softening contribution of the transformation as a deformation mechanism and a hardening contribution of the transformation product. Stress-assisted transformation gives plastic flow at stresses lower than the normal slip-controlled yield stress, and produces a reverse (positive) temperature dependence of the yield stress. The temperature where the transformation yield stress and slip yield intersect, characterized by a reversal in the yield-stress temperature dependence, is designated M_s^σ, and its value measured in uniaxial tension serves as a convenient measure of overall austenite stability with respect to mechanically induced transformation. As the transformation volume change interacts with the hydrostatic component of stress, the austenite stability and M_s^σ temperature vary significantly with stress state.

The upward σ–ε curvature associated with transformation plasticity imparts high stability to plastic flow behavior which is found to retard not only tensile necking but shear localization both within tensile necks and at crack tips. Figure 14 summarizes the measured effect of austenite stability (controlled by test temperature) on the relative change in a) uniform ductility, ε_u, b) tensile fracture ductility, ε_f, and c) J_{IC} fracture toughness, in high-strength (1300 MPa σ_y) γ'-strengthened austenitic steels (77,78). The stability variable θ represents a normalized temperature defined by $\theta = (T-M_s^\sigma)/(M_d-M_s^\sigma)$ such that $\theta = 0$ corresponds to M_s^σ, and $\theta = 1$ corresponds to $T = M_d$, the highest temperature for which strain-induced transformation occurs. Here the M_s^σ temperature corresponds to that for the particular stress state controlling the property of interest. In addition to

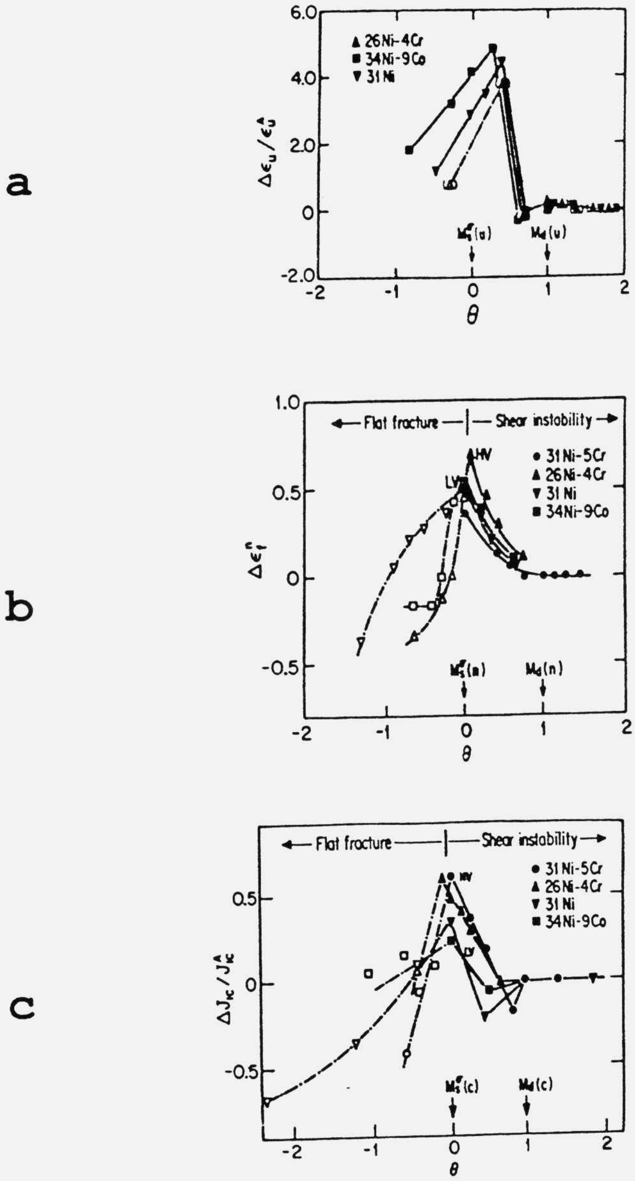

Fig 14. Relative mechanical property enhancement vs. transformation stability represented by normalized temperature, θ, for precipitation-strengthened metastable austenite steels. (a) increase in uniform ductility $\Delta\varepsilon_u$ relative to stable austenite value ε_u^A, (b) increase in true fracture strain ε_f^n in axisymmetric tension, (c) increase in fracture toughness ΔJ_{IC} relative to stable austenite value J_{IC}^A, with LV and HV denoting low and high volume-change alloys, respectively (77, 78).

the well known effect of transformation on uniform tensile ductility, the results of Figure 14 demonstrate strong enhancement of ε_f and J_{IC} in materials where both failure initiation in the tensile neck and sharp-crack propagation are controlled by shear localization. Property enhancement is extremely sensitive to stability, with optimum properties achieved near the M_s^σ temperature. Hence, efficient use of transformation plasticity to improve a property at a given temperature requires placement of M_s^σ (for the stress state governing that property) at the temperature of interest. The precise mechanism by which transformation plasticity enhances J_{IC} toughness is being investigated by detailed metallographic observations of crack tip shear localization and transformation behavior (79) coupled with finite-element modelling of crack-tip transformation plasticity based on the transformation-kinetics-based constitutive models (80).

Composite systems with metastable austenite dispersions can exhibit essentially the same transformation plasticity features as fully austenitic alloys. The stability and transformation plasticity behavior of dispersed austenite in high strength steels has been most thoroughly investigated in the case of retained austenite in Stage I tempered 4340 steel (32,81-83). For both 870C and 1200C austenitizing temperatures, controlled experiments varying austenite content with high magnetic field cryogenic treatments prior to 200C tempering have separated the role of the austenite in mechanical behavior. Microyielding experiments have quantified the retained austenite stability by measuring its M_s^σ temperature in uniaxial tension and compression, and revealed microyield σ-ε behavior consistent with transformation plasticity model predictions (82). The measured stress-state dependence of M_s^σ revealed an M_s^σ near room temperature for pure shear, and room temperature shear tests confirmed a significant increase in the shear instability strain, γ_i, from transformation plasticity interaction. The measured stability also indicated too low a stability level for optimum toughening interaction at a mode I crack tip, and controlled experiments confirmed that there was no significant effect of the retained austenite on K_{IC} toughness (81). The high stress levels operating in such high-strength steels contribute a large mechanical driving force for transformation. Achieving sufficiently high stability against transformation to obtain optimal toughening interaction is likely beyond the capabilities of the simple carbon-partitioning-based stabilization operative in the conventional retained austenite of Stage I tempered martensitic steels.

Martensitic nucleation theory (84) prescribes the manner in which particle size and composition control the stability of dispersed austenite. Size influences stability through the statistical behavior of heterogeneous nucleation sites. In metals and ceramics, a universal form of nucleation site potency distribution (85,86) defines the manner in which characteristic defect potency diminishes with decreasing particle size. Composition affects stability in the same manner as for bulk materials, through the transformation chemical driving force and through a solid solution hardening effect on interfacial mobility (85). The high levels of austenite stability necessary for optimal transformation toughening in ultrahigh strength steels can thus be attained by a combination of particle size refinement and enrichment in stabilizing solutes. The precipitation of austenite during tempering of secondary hardening steels offers the means to achieve this microstructural objective.

Multistep tempering treatments have demonstrated the ability to effect the desired microstructural control. Austenite stabilization also forms the central concept of "triple phase" ferrite/martensite/austenite low-alloy sheet steels designed to achieve sufficient plane-strain uniform ductility (20-25%) for adequate stretch formability at high strength levels (100ksi 3% flow strength) desired for automotive applications (87). Short-time intercritical tempering after a low temperature temper which enriches cementite in Mn can produce a paraequilibrium carbide→austenite conversion, trapping a higher-than-equilibrium Mn content in the austenite (88). While this austenite normally forms at martensite lath boundaries where rapid growth ensues, thermodynamic calculations employing the paraequilibrium constraint can predict optimal cementite Mn contents and intercritical tempering temperatures to promote intragranular carbide conversion in recrystallized structures to achieve finer dispersions with higher stabilizing Mn contents (87). Similarly, in the high alloy AF1410 secondary hardening steel, solute enrichment of cementite at 420C prior to 510C tempering has been shown to provide a finer, more solute enriched (intralath) austenite compared with the interlath austenite which precipitates during conventional single-step 510C tempering (83).

While optimal austenite stabilization in the low alloy steels requires trapping of Mn levels higher than equilibrium, the interlath austenite that precipitates during conventional tempering of high alloy steels like AF1410 involves incomplete partitioning such that the austenite solute content is lower than the equilibrium level, and further stabilization can be achieved by moving closer to equilibrium. In this case, more effective than cementite nucleation of austenite is the use of a short high temperature treatment prior to 510C tempering, which is found to nucleate a fine intralath dispersion of near-equilibrium austenite (83). The open symbols in Figure 15 show Charpy toughness/hardness combinations achieved by various temperature(°C)/time(minutes) treatments prior to 510C/8 hr tempering in AF1410; also shown are the properties (solid symbols) for conventional 510C tempering for 5 and 8hrs. The curves represent contours of a quality parameter reflecting the normal hardness dependence of Charpy toughness. At R_c48 hardness, the 600C/15min. treatment provides a 24% toughness increase, while 570C treatments offer even better hardness/toughness combinations. Figure 16 shows a transmission electron micrograph of the microstructure produced using the 600C/15min treatment (83). While relatively coarse interlath austenite (similar to that formed with single-step 510C tempering) is present, a fine intralath dispersion of 10-20nm austenite particles is also evident throughout the structure. Austenite compositions determined by STEM microanalysis of this structure are compared with

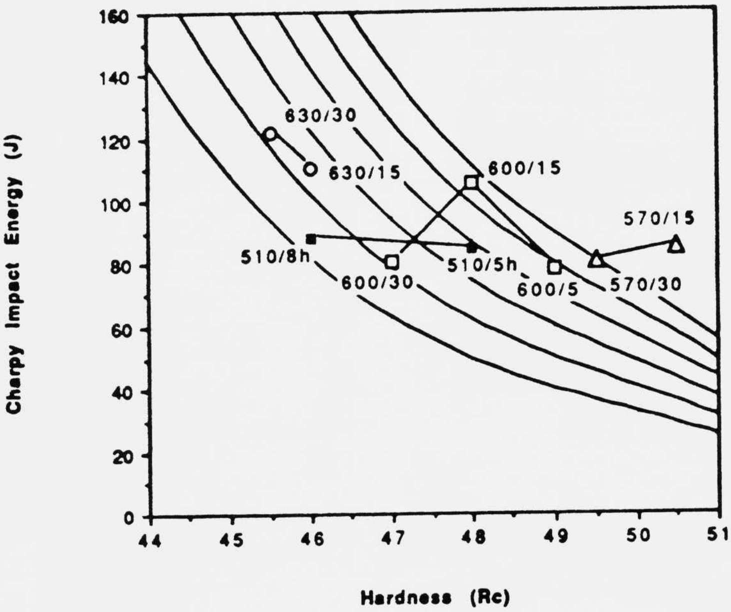

Fig. 15 Charpy V-notch impact toughness vs. hardness achieved by multistep heat treatment to form high stability austenite in AF1410 steel. Open symbols denote properties for indicated temperature (°C)/time (minutes) treatments prior to 510C/8 hr tempering. Closed symbols denote properties for conventional 510C tempering for 5 and 8 hrs (83).

those for single-step 510C (5 and 8hr) in Table 4, together with associated mechanical properties. In addition to the substantial size refinement, it is evident that the Ni content is much increased in the fine austenite nucleated at 600C, and is close to the predicted equilibrium composition (82). Whether compared to single-step 510C tempered materials on the basis of constant hardness (510C/5hr) or yield strength (510C/8hr), it is clear from the properties listed in Table 4 that the achievement of an optimal austenite stability level has produced a substantial improvement in J_{IC} fracture toughness; equivalent to a K_{IC} of 230 ksi$\sqrt{in}$, this corresponds to a record toughness for a steel of R_c48 hardness.

Fig. 16 TEM micrograph showing fine dispersion of intralath austenite formed by multistep heat treatment (600°C/15 min + 510°C/8 hr); larger interlath austenite is also evident (83).

TABLE 4

AF1410
PRECIPITATED-AUSTENITE TRANSFORMATION TOUGHENING

	510C/5h	510C/8h	600C/15min+510C/8h
γ MICROSTRUCTURE			
Composition			
interlath: (0.1-0.2mm)		14Ni-13Co-3Cr	17Ni-15Co-4Cr
intralath: (100-200Å)		---	29Ni-10.5Co-4Cr
f^{γ}	0.03	0.06	0.15
PROPERTIES			
Hardness	R_C48	R_C46	R_C48
Yield Strength	1550 MPa	1360 MPa	1370 MPa
J_{IC} Toughness	178 kJ/m^2	201 kJ/m^2	250 kJ/m^2

Experiments in two series of model high-strength (R_c45) austenitic alloys strengthened by γ' precipitation and phosphocarbide precipitation have allowed a separation of the relative roles of transformation strain hardening and transformation dilatation in transformation toughening under condition of shear-localization-controlled ductile fracture (89). In the phosphocarbide-strengthened material, comparison of underaged and overaged material of the same hardness allows variation of transformation strain hardening behavior by altering the austenite/martensite hardenss difference. Due to preferential martensite hardening by dissolved carbon, the underaged material has an austenite/martensite Vickers hardness difference of $\Delta H_v=88\pm2$ while the overaged material has $\Delta H_v=47\pm2$ identical to the γ'-strengthened alloys. Variations in Ni and Cr content provide variations in transformation dilatation. Figure 17 shows the transformation toughening efficiency determined in these alloys as the ΔJ_{IC} toughening increment per amount of crack-tip transformation measured as the transformation half-zone height, H/2. The curves indicated for the two ΔH_v levels suggest that higher transformation strain hardening enhances toughening, but a more dramatic effect is that toughening increases as the third power of the transformation dilatation; this behavior of transformation toughening in ductile solids contrasts with a second power dependence of crack-tip shielding-based transformation toughening in brittle solids (90). The strong dilatation dependence suggests that much more toughening can be achieved from precipitated austenite in secondary hardening martensitic steels by designing the austenite for maximum dilatation.

Although the composition dependence of the transformation dilatation is highly nonlinear due to magnetic anomalies in austenite, magnetic models have been applied to its prediction (91). Such models are being calibrated by precision lattice parameter measurements in key compositions, to be applied in the design of optimal precipitated austenite for transformation toughening (92).

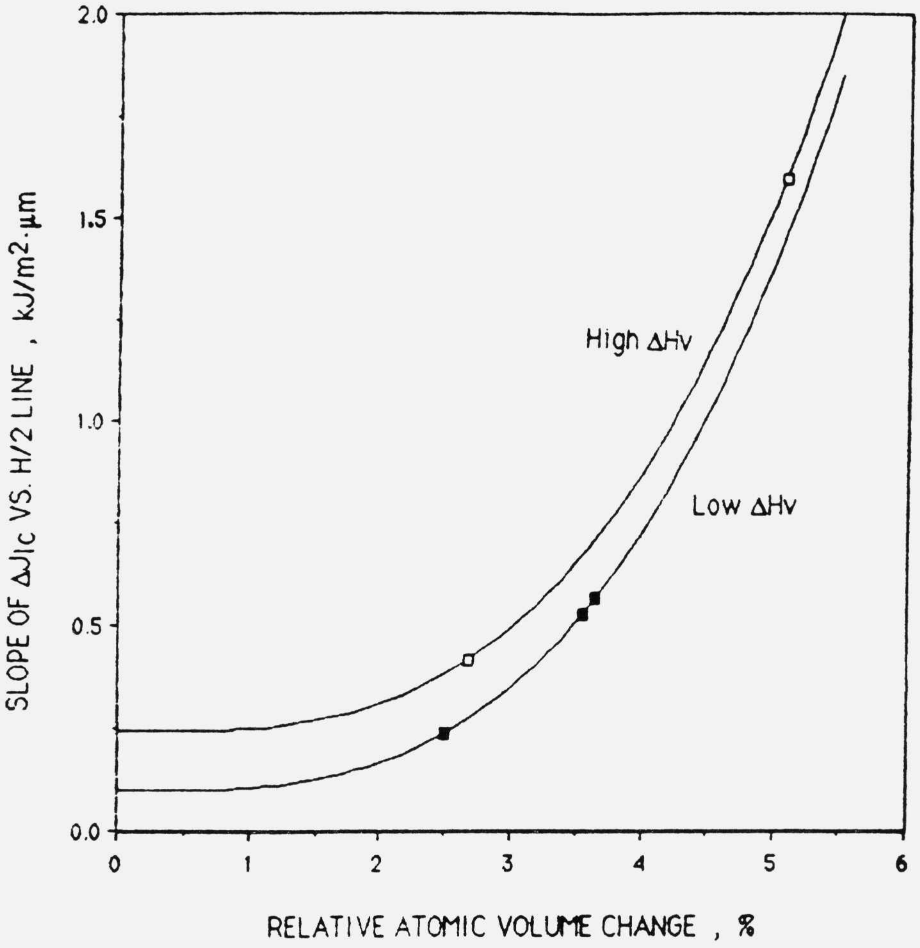

Fig. 17 Transformation toughening efficiency (slope of ΔJ_{IC} vs. transformation zone half-height, H/2) vs. transformation volume change for precipitation-hardened metastable austenitic steels with two levels of austenite-martensite hardness difference, ΔHV (89).

HYDROGEN RESISTANCE AND INTERFACIAL COHESION

The stress corrosion cracking of ultrahigh-strength martensitic steels in aqueous environments, as quantified in standard K_{ISCC} tests, is known to occur by a hydrogen embrittlement mechanism associated with cathodic charging at the crack tip. Typical of hydrogen-assisted cracking at extreme strength levels, the fracture generally follows an intergranular path and is commonly associated with prior intergranular segregation of embrittling impurities. As discussed by McMahon (93), these are the same impurities responsible for the phenomenon of intergranular temper embrittlement, and extensive studies have revealed the relative embrittling potencies of impurities (e.g. P, S, Sn, Sb) and embrittling alloying elements (e.g. Mn, Si), as well as separating the role of cosegregating alloying elements which can alter the degree of impurity segregation. Thusfar, the embrittling effect of hydrogen and prior segregants appear to be additive, and a common mechanistic basis can be sought for interfacial embrittlement by chemical segregants including hydrogen.

A general theoretical framework for treating the chemical embrittlement of interfaces has been developed by Rice and coworkers (94, 95) who have modelled the competition between brittle interfacial cleavage separation and crack-tip blunting by dislocation emission. Considering a flat crack in a bicrystal interface, the conditions for ductile vs. brittle crack advance are determined by comparison of (a) the critical crack extension force (strain energy release rate) G_{disl} for crack-tip dislocation emission, as governed by crystal plasticity, and (b) the Griffith work of interfacial cleavage, $2\gamma_{int}$, as influenced by chemical segregation. Brittle propagation prevails when $G_{disl}>2\gamma_{int}$, and ductile when $G_{disl}<2\gamma_{int}$. For fixed $2\gamma_{int}$, model calculations predict that G_{disl} will depend on the direction of crack advance, such that brittle fracture can occur for one direction while ductile behavior occurs for the opposite direction. The prediction has been confirmed in critical bicrystal experiments on Cu embrittled by Bi (95).

While the precise manner in which chemical segregants might modify G_{disl} for dislocation emission remains unclear, a definite role of segregation in determining the Griffith work of interfacial cleavage $2\gamma_{int}$ has emerged from application of surface thermodynamics. Further, arguments have also been developed that $2\gamma_{int}$ is not only of crucial importance in governing the transition between ductile and brittle response, but even under conditions of substantial crack-tip plasticity the critical crack-extension force G_{IC} for intergranular fracture can be a monotonic function of $2\gamma_{int}$ (94). Control of $2\gamma_{int}$ would thus appear the most effective means of enhancing interfacial fracture resistance. The thermodynamic analysis (94, 95) reveals that for interfacial separation at fixed boundary solute coverage, Γ, nonlinear entropy contributions can be neglected such that $2\gamma_{int}$ changes linearly with Γ according to the relation:

$$2\gamma_{int} = (2\gamma_{int})_o - (\Delta g_b^o - \Delta g_s^o)\Gamma$$

where $(2\gamma_{int})_o$ is the work of separation of the clean interface, and Δg_b^o and Δg_s^o are the free energies of segregation of the solute to the boundary and free surface, respectively, evaluated at the temperature of fracture, taken as 300K. The analysis clearly predicts that a segregating solute with a greater (more negative) segregation energy at a free surface compared to an internal boundary will embrittle (reduced $2\gamma_{int}$), while one with a lower energy at a boundary compared to the free surface will enhance interfacial cohesion (increased $2\gamma_{int}$). The embrittling potency of a segregant scales with the quantity $\Delta g_b^o - \Delta g_s^o$. The model further predicts that an embrittling solute which is mobile during fracture such that it can maintain a constant potential μ during separation will be far more embrittling than for the case of separation at fixed Γ (immobile solute).

The relative wealth of surface thermodynamic data (determined primarily from Auger electron spectroscopy studies) available for iron and steels compared to other materials make iron-based alloys the best case to test thermodynamic theory of interfacial cohesion. Unfortunately, however, both the grain boundary and free surface quantities are anisotropic, and insufficient data is available to either compare Δg_b^o and Δg_s^o at a fixed orientation or to apply consistent directional averaging procedures. Nevertheless, chemical trends are evident when $\Delta g_b^o - \Delta g_s^o$ is estimated from the available data for embrittling impurities. The best current measure of embrittling potency is the shift of the intergranular ductile-brittle transition temperature per amount of segregated solute (expected to depend linearly on $2\gamma_{int}$) and available measurements of this quantity are plotted vs. $\Delta g_b^o - \Delta g_s^o$ in Figure 18 (94). Despite considerable uncertainty associated with the available mix of polycrystalline and single crystal data, the predicted trend represented by the solid line is supported, particularly for the more well-defined cases of P and S. More recent

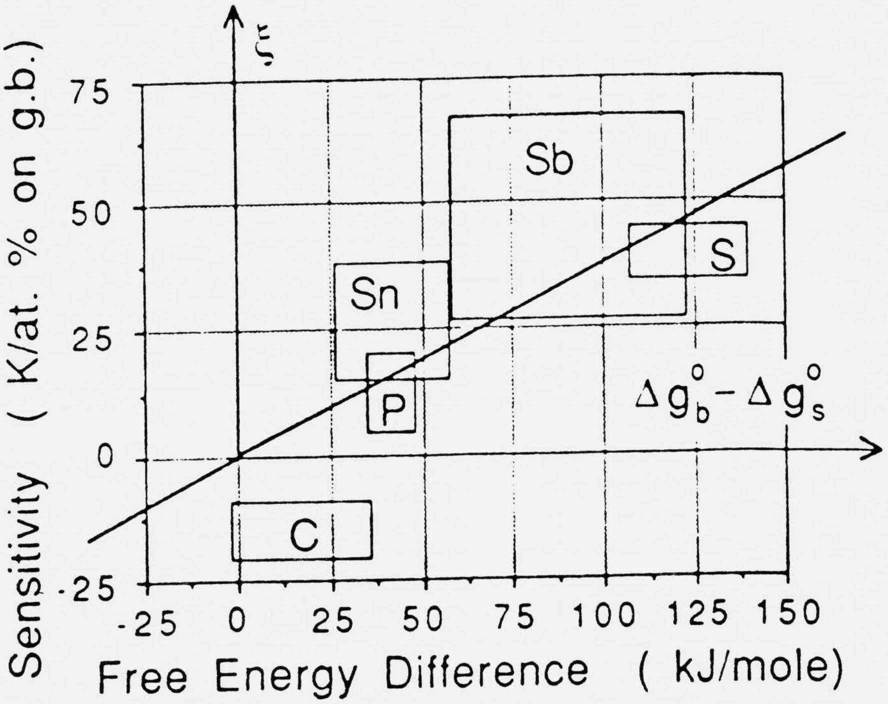

Fig. 18 Embrittling potency of impurity segregants in iron and steel (shift of transition temperature per amount of segregant) vs. difference in segregation free energies to grain boundaries Δg_b^o and free surfaces Δg_s^o (94).

thermodynamic data for B also correlate with its measured cohesion-enhancing effect (96). Estimates of Δg_b^o - Δg_s^o for H indicate an intrinsic embrittling potency less than or equal to that of P (95). The high mobility of H can allow separation at constant μ, however, and calculations for this case (95) predict substantial reduction of $2\gamma_{int}$ even for equilibrium matrix concentrations of $X_H \approx 10^{-9}$; the model is thus consistent with the extreme effectiveness of H as an embrittler (93).

A plausible thermodynamic description of the chemical embrittlement of interfaces opens the way to a more fundamental approach whereby first-principles quantum-mechanical calculations of the electronic state of impurities in grain boundary and corresponding fracture surface environments can provide insight into the origins of

$\Delta g_b^o - \Delta g_s^o$ in chemical bond behavior, offering the potential for design of boundary composition for both enhanced intrinsic cohesion and reduced hydrogen interaction. The relatively low intrinsic embrittling potency represented by $\Delta g_b^o - \Delta g_s^o$ for P and H, which are the most common embrittlers of the highest strength steels, offers hope of neutralizing their embrittlement or even reversing their role to cohesion enhancement through appropriate boundary doping to achieve desired boundary electronic structure. While the most advanced techniques such as the Full-Potential Linearized Augmented Plane Wave (FLAPW) method (97) now appear capable of computing the relatively small energy differences governing metallurgical phenomena, the crucial first step in applying such techniques is to obtain realistic atomic positions for the structures of interest.

As reviewed by Harrison et al (98), simple hard-sphere models of grain boundary structure have revealed a striking similarity between the special polyhedral packing units present in grain boundary cores and the local coordination environments adopted by the light metalloid elements (e.g. B, C, P, S) in metal-rich transition metal compounds such as Fe_3P, as well as their coordination environments in metallic glasses. Specifically, these elements adopt the nine-fold coordination of a capped trigonal prism which is a common structural unit in tilt boundaries. Harrison et al (98) have simulated the core structures of several high coincidence tilt boundaries chosen to allow relatively short-period supercells appropriate for band-theory-based electronic calculations. To examine local atomic relaxations, a simple interatomic potential for Fe was derived based on the embedded atom method (EAM) and tested against observed free surface relaxations in Fe*. The model was initially applied to a $\Sigma 5$ [100] tilt boundary on (031). Full occupancy of the trigonal prism sites of this boundary by P, however, would involve a minimum P-P spacing of 2.87Å which is shorter than the minimum P-P distance of 3.48Å exhibited in Fe_3P.

---

*Although the ability to predict observed oscillitory variations in interplanar spacings at free surfaces is often used as an assessment of the validity of these potentials, they found such variations to be relatively insensitive to details of the potential, and found no better agreement with the observed surface relaxations of Fe than could be predicted from a simple model based on electrostatic effects neglected in the EAM approximations.

Furthermore, chemisorption of P on a (100) Fe surface, where the minimum site spacing is 2.87Å, is observed to involve a c(2x2) surface reconstruction maintaining a minimum P-P spacing of 4.05Å. A survey of possible boundaries allowing a minimum period supercell with full P site occupancy led to selection of the $\Sigma 3[1\bar{1}0]$ "incoherent" twin boundary on (111); the P site spacing of 4.05Å is greater than the minimum P-P distance in Fe_3P, and P chemisorption on the corresponding (111) Fe free surface involves a simple p(1x1) structure with full site occupancy. The relaxed structure for this boundary computed with the Fe EAM potential is shown in the supercell of Figure 19. Viewed along the $[1\bar{1}0]$ tilt axis, the two sizes of open circles represent the two stacking positions of $(1\bar{1}0)$ planes. The solid rectangles outline the projected positions of BCC units cells in the two grain orientations, and the capped trigonal prism 9-fold coordination sites are outlined in solid and dashed lines with solid circles depicting schematically the position of P sites. Repetition of supercells such as that outlined in Figure 19 provides the necessary periodic structure for band-theory-based electronic calculations.

As a first assessment of the ability of band calculations to treat the chemical aspects of brittle fracture in transition metals, Krasko (99) has applied the Linear Muffin Tin Orbitals-Atomic Spheres Approximation (LMTO-ASA) method to the classical problem of the effect of Ni on the resistance of Fe alloys to (100) cleavage fracture, using a simple periodic supercell in which vacuum is represented by empty atomic spheres to simulate (100) free surfaces. Using unrelaxed surface structures in which bulk interplanar spacings are rigidly maintained, the calculations overestimate the magnitude of the free surface energy, but clearly demonstrate that Ni at positions both on the free surface and one plane below substantially raise the (100) surface energy and therefore increase the Griffith work of separation. A decomposition of the surface energy change into magnetic and chemical contributions shows that while the strong effect of Ni below the surface is chemical in nature, the effect of Ni on the surface plane is entirely a magnetic effect arising from suppression of the normally enhanced magnetic moment of Fe atoms on a (100) surface which significantly reduces the surface energy and (100) cleavage resistance of pure Fe.

An initial application by Krasko (100) of the LMTO-ASA method to the Fe grain boundary of Figure 19 has indicated that the near neighbor Fe atom separations across the boundary predicted by the EAM potential are unrealistically small. A modified EAM potential incorporating an explicit magnetic energy function is being developed (101) using

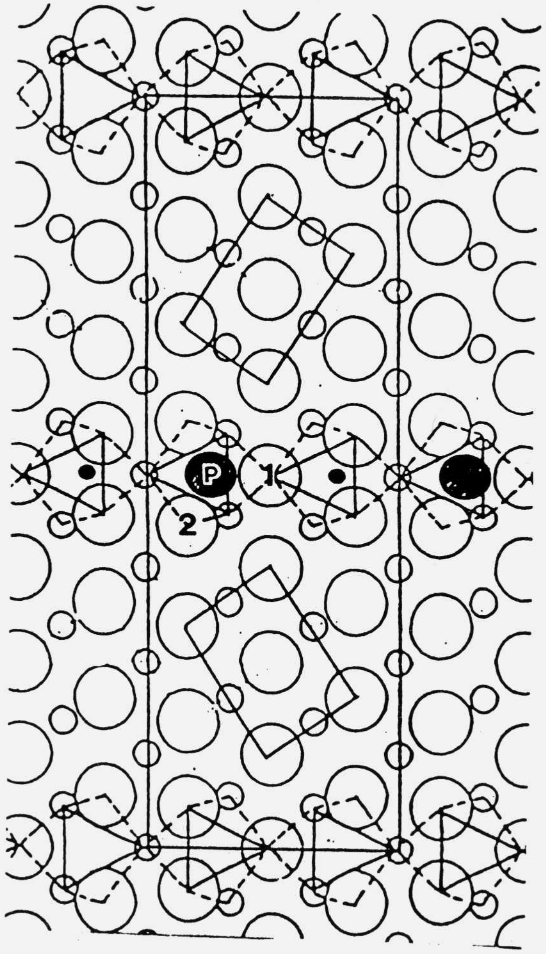

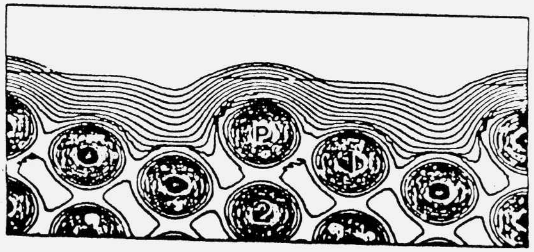

Fig. 19 Configurations employed in electronic calculations for P in Fe at grain boundary (left) and corresponding free surface (above) environments; free surface includes computed charge density contours (100, 103).

results of LMTO-ASA calculations for large strain deformation of Fe between BCC and FCC structures (102). Preliminary LMTO-ASA calculations have been performed for the $\Sigma3[1\bar{1}0](111)$ Fe tilt boundary containing P using a smaller 6-layer supercell in which the interplanar spacing of the first two (111) planes at the boundary core are adjusted to maintain the Fe-P bond distances of the Fe_3P structure (100). The energy and electronic structure have been compared with and without P, holding the Fe atom configurations fixed. Comparison with the state of P on the corresponding (111) fracture surface is made possible by a preliminary FLAPW calculation performed for this case by Li and Freeman (103). Upon fracturing the boundary, the P atom can relax out of the plane of the grain boundary central Fe atoms (#1 in Figure 19) to a position like that represented in the computed charge density plot at the right of Figure 19. In this preliminary calculation, the Fe-P distance was arbitrarily set equal to the Fe-Fe near neighbor distance.

Consistent with the expected electronegativity difference, the FLAPW calculation indicates charge transfer from Fe to P on the (111) free surface. In contrast, the LMTO-ASA calculation for P in the confined environment of the grain boundary indicates that the P atom (as defined by its Wigner-Seitz sphere volume) is charge deficient, and integration over this volume of the charge density difference relative to the superimposed charge densities of the clean Fe boundary and a pure P monolayer indicates a net transfer of ~0.1 electron from P. Such reverse charge transfer is consistent with the findings of other calculations for metalloid impurities in solid metallic environments and runs counter to the proposal of Briant and Messmer (104) based on simple cluster calculations that impurity-induced embrittlement is associated with weakened Fe-Fe bonding through charge transfer from Fe to the impurity. As is typical of free surfaces, the FLAPW calculations indicate the outer Fe atoms on the clean free surface are deficient 0.24 electron. Adsorption of a P monolayer restores 0.2 electron to these Fe atoms, and increases the Fe work function from 4.7 to 5.5 eV indicative of strong Fe-P bonding. The reversal of Fe-P charge transfer to a more natural state on the free surface and the restoration of surface Fe charge through P interaction may contribute to a lower energy of P on the free surface compared to the grain boundary. Energy comparisons will require relaxations of the surface P configuration, and a meaningful assessment of the role of charge transfer will require a more detailed analysis of the spatial redistribution of charge.

In analogy to the findings for the effect of Ni on Fe (100) cleavage resistance, an assessment of possible magnetic contributions to P embrittlement can be sought from the calculated Fe magnetic moments in the grain boundary and free surface environments. In both environments, Fe atom #1 of Figure 19 in the absence of P shows an enhanced magnetic moment of ~$2.8\mu_B$ compared to $2.2\mu_B$ for bulk BCC Fe. Segregated P lowers the moment of this Fe atom in both environments, but more so in the grain boundary (~$1.1\mu_B$) than on the free surface (~$2.2\mu_B$). A lower magnetic free energy might thus contribute to the lower energy of P on the free surface vs. the grain boundary.

Holding the Fe atom configuration the same as that adopted for the Fe-P case, a preliminary comparison of the states of B, C, P, and S in the grain boundary environment has been conducted with the LMTO-ASA method (100). The reverse charge transfer and strongly reduced Fe magnetic moment are similar for P and S, while weaker effects are found for B and C. Projected density of states (DOS) curves for the Fe atom adjacent to the boundary in Figure 19 are directly compared with reflected (negative) DOS plots for the impurity atoms in Figure 20. Overlap between the B and C 2p bands and the Fe 3d band in the region ~0.3 R_Y below the Fermi level, E_F, allows for strong Fe-impurity bonding, while such overlap with the 3p bands of P and S is virtually absent. These features, together with the relative magnetic moments and charge transfers, are in line with the greater boundary segregation energies for B and C compared to P and S. The relatively poorer bonding of P and S to the grain boundary offers the potential for a more profound change of bonding character on moving to the less constrained free surface environment.

An application of the simpler layer Korringa-Kohn-Rostoker (LKKR) technique to the Fe-P $\Sigma3[1\bar{1}0](111)$ boundary reproduces qualitative features of the more rigorous LMTO-ASA results, including the relative reduction of the boundary Fe magnetic moment by P (105). Some preliminary calculations (106) using the Discrete Variational-X_α (DV-X_α) embedded cluster technique (107) have allowed direct comparison of the state of P in the Fe grain boundary and free surface configurations using the same atomic positions employed in the LMTO-ASA and FLAPW calculations. While the 3p component of the P DOS shows a similar shape to that in Figure 20 for the grain boundary case, the shape distorts in the free surface case favoring energies near E_F which may reflect enhanced Fe-P interaction. Once essential electronic features of embrittlement are determined using the more rigorous LMTO-ASA and FLAPW methods, these simpler techniques may allow a quicker investigation of alloying effects as the basis of alloy design for enhanced interfacial cohesion.

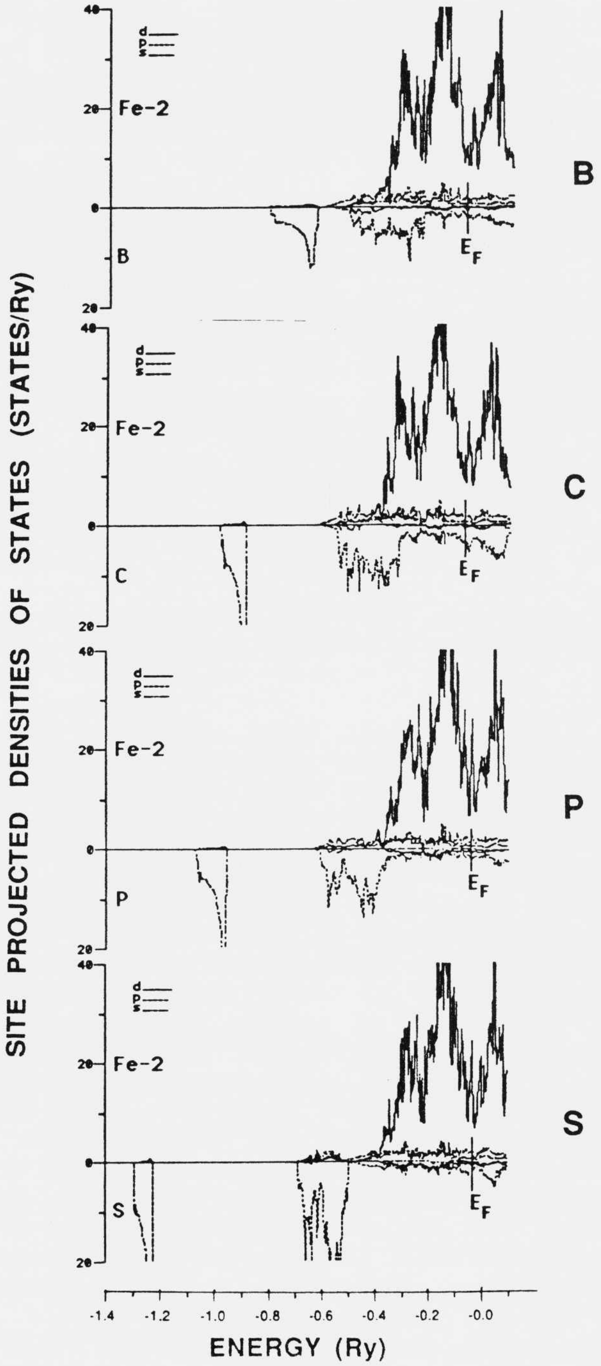

Fig. 20 Density of states (DOS) curves for the Fe atom adjacent to boundary of Figure 19, directly compared to reflected (negative) DOS plots for B, C, P, and S in impurity site (100).

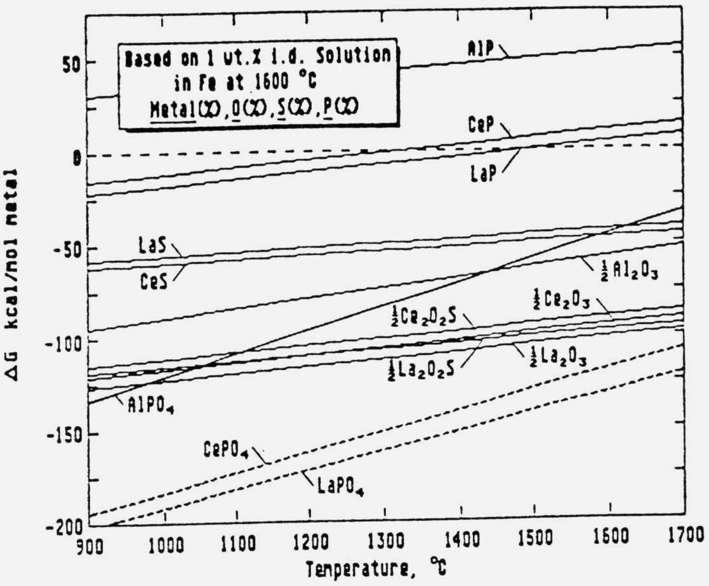

Fig. 21 Estimated free energy of formation (from solution in Fe) of potential impurity gettering phases (108).

While an electronic level understanding of interfacial embrittlement offers the greatest potential for property improvements in the long term, more immediate improvements based on empirical knowledge have been achieved through novel techniques for gettering of known embrittling impurities, and through constraint of alloy composition to exclude known embrittling alloying elements. Studies of rapid solidification phenomena in steels mentioned earlier (65, 71) have revealed that in addition to a substantial refinement in the particle size of "inclusion" phases, the normal sequential formations of oxides and sulfides is replaced by complex oxysulfide formation at the high melt undercoolings achievable by rapid solidification. Compared to sulfides, these phases getter sulfur in a much more stable form which resists dissolution at extreme temperatures. Phosphorus is normally very difficult to getter in conventionally processed steels due to the much lower stability of phosphides relative to sulfides. To explore the possibility of extending the rapid solidification effect to the formation of stable oxygen-phosphorus compounds, a thermodynamic survey was conducted of the potentially most stable phosphorus and sulfur gettering compounds in steels (108). Figure 21 summarizes the estimated free energy of formation of such compounds from dilute solution in Fe, plotted vs. temperature in the range 900-1700°C, identifying lanthanum as the most promising alloy addition to getter P as $LaPO_4$ and S as La_2O_2S.

Thermodynamic and kinetic modelling further indicated feasibility of forming the metastable $LaPO_4$ phase at high melt undercoolings in compositions with the P and S contents of typical high quality steels, provided oxygen is kept sufficiently low (108). The high stability of such compounds should also provide the necessary coarsening resistance for an effective grain refining dispersion (once finely dispersed by rapid solidification) while their high cohesive energy should also in principle contribute interfacial cohesion (and microvoid nucleation resistance) through a high particle-phase free surface energy.

A simple stage I tempered martensitic steel composition was then designed as a substitute for 4340 steel capable of equivalent strength and toughness, but excluding Mn, Si and Cr for enhanced interfacial cohesion. Carbon was maintained at 0.40C for strength, a comparable nickel content of 2.0Ni was held for cleavage resistance, and molybdenum (a possible cohesion enhancer) was increased to 1.5Mo for equivalent hardenability. Rapid solidification processing was performed by remelting a well-deoxidized billet of this composition, followed by a late addition of $LaNi_5$ (balanced to the melt P and S content with an empirical loss factor) just prior to rapid solidification via centrifugal atomization. A modest quantity of powder was produced and consolidated by hot extrusion at 1100°C. STEM microanalysis employing a windowless Xray detector revealed particles of the type shown in Figure 22 with an Xray fluorescence spectrum confirming the presence of La, O, and P; finer particles containing La, O, and S and presumed to be La_2O_2S were also observed. The presence of the La-O-P phase after 1100°C consolidation and its relatively fine ~0.1μm size attests to a high stability of the compound. Observations on as-solidified powder by Hayzelden (60) confirms the presence of similar particles, but quantitative STEM microanalysis reveals a much higher O/P ratio than that of $LaPO_4$ suggesting an "oxyphosphide" phase rather than phosphate.

Despite serious powder cross-contamination, the experimental steels exhibited K_{IC} toughness superior to conventional 4340 and a reduced degree of quasicleavage fracture. Due to a higher-than-specified carbon content, a hardness of R_c57 was achieved with stage I tempering at 200°C, and the grain coarsening resistance associated with the stable particle dispersions was also demonstrated. Although the small amount of material did not allow adequate K_{ISCC} determination, a rising-load K_{ISCC} screening test for which 4340 steel failed at 10 ksi$\sqrt{in}$ indicated a K_{ISCC} of 40 ksi$\sqrt{in}$, and a standard K_{ISCC} specimen survived 10^3 hr at 20 ksi$\sqrt{in}$ without failure. The K_{ISCC} levels indicated by these

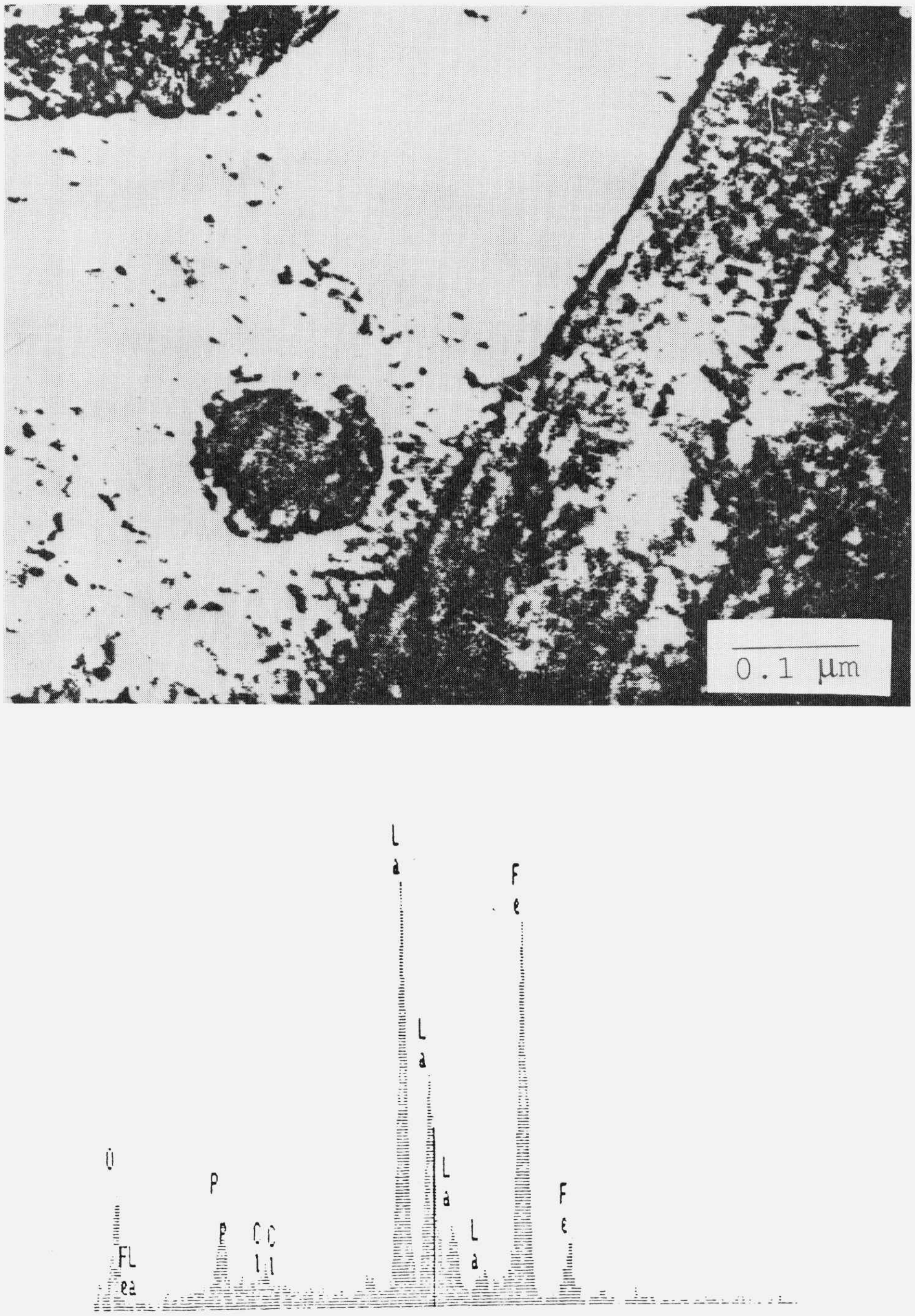

Fig. 22 STEM micrograph and associated X-ray fluorescence spectrum of La-O-P particle in rapidly solidified LaNiMo steel after consolidation at 1100C (108).

preliminary experiments are compared against conventional ultrahigh-strength steels in Figure 23, indicating a major property advance associated with achievement of the designed microstructure.

A larger heat of the experimental steel has been produced by gas atomization (109), but STEM microanalysis revealed the presence of lanthanum silicates attributed to a crucible reaction, with no evidence of the desired P and S gettering phases. Strength and toughness equivalent to 4340 was obtained, with good ballistic properties, but a measured 10^3 hr K_{ISCC} of only 7 ksi$\sqrt{in}$ confirms the necessity of the impurity gettering to achieve the remarkable stress corrosion resistance (110). Another gas-atomized heat produced with appropriate processing modifications is currently being evaluated (110).

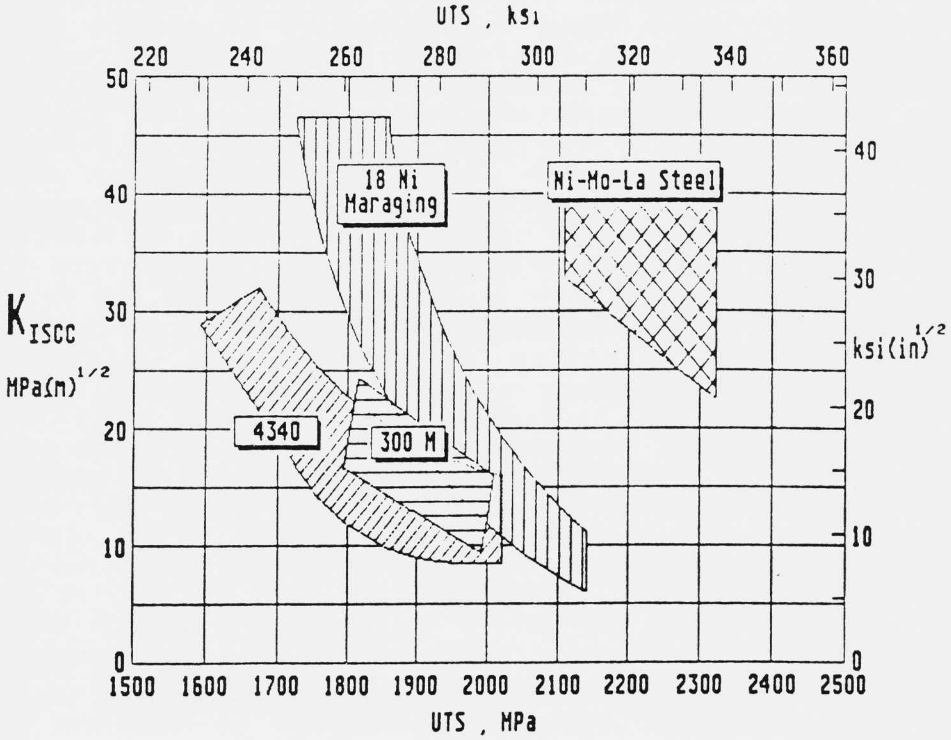

Fig. 23 Stress-corrosion resistance vs. strength comparing rapidly solidified LaNiMo steel with conventional ultrahigh-strength steels (108).

MATERIALS DESIGN: STAINLESS BEARING STEEL

Our first effort to integrate these developments into the design of one alloy was undertaken by a team of students in the Materials Design Course at Northwestern University (111), who performed a conceptual design of a stainless bearing steel for the Space Shuttle Main Engine turbopumps, a demanding application requiring substantial improvements in toughness and stress-corrosion resistance. Maintaining a R_c60 hardness level required for rolling contact fatique resistance and wear resistance, property objectives consisted of a doubling of K_{IC} and K_{ISCC} relative to the current alloy 440C employed in this application. Consistent with the system framework of Figure 2, a sequence of calculations was devised to arrive at a unique alloy composition tailored to achieve quantitative microstructural objectives under specific processing conditions. For stress corrosion resistance, the overall composition was first constrained for compatability with rapid solidification processing and La treatment, with exclusion of Mn and Si for interfacial cohesion. An Orowan strengthening analysis was applied to the available hardness and particle size data from the experimental steels of Table 1, defining the necessary particle spacing for R_c60 hardness, and a minimum carbon content of 0.30C was estimated to achieve this condition. Matrix composition was constrained to include 12Cr for stainless properties. THERMOCALC computations were then employed to compute a line of compositions in Ni and Co that maintained a sufficiently high M_s temperature to give the desired lath martensite structure. To incorporate transformation toughening, a unique Ni and Co composition was determined by the nature of the austenite that would precipitate during tempering near 500C, both in terms of its amount and its transformation stability as quantified by the martensitic transformation driving force at room temperature. To achieve maximum strengthening efficiency without embrittlement following the considerations of Figure 6, V and Mo contents were then optimized to maximize the driving force for coherent M_2C at 500C while maintaining limits on the M_6C and $M_{23}C_6$ carbide driving forces, subject to a maximum allowed solution treatment temperature. A second iteration of this complete sequence was then followed to achieve self consistency.

In this manner, a computer-aided thermodynamics-based design yielded a unique seven component alloy composition which is thermodynamically (and kinetically) capable of achiéving a desired multiphase microstructure under fairly well prescribed processing conditions. A small heat of this composition has been prepared and is currently undergoing evaluation. If this prototype alloy is successful, we will have arrived at a very different way of creating new materials.

SUMMARY

Advances in theory and instrumentation focused on the principles underlying control of strength, toughness, and hydrogen resistance in ultrahigh-strength steels have achieved a level of fundamental understanding allowing true materials design. A comprehensive combined SANS, TEM, APFIM, STEM investigation of M_2C carbide precipitation has demonstrated important predicted features of precipitation at high supersaturation, and identified major effects of particle coherency. Recent theory of coherent thermodynamics and multicomponent diffusional kinetics calibrated by nanoscale experimental measurements has allowed application of the THERMOCALC thermochemical database and software system to predict the alloy composition dependence of basic scaling factors governing precipitation behavior. The thermodynamics-based control of competing precipitation reactions then allows design of optimal compositions for efficient strengthening without embrittlement.

Novel shear tests conducted in materials with well characterized particle dispersions have quantified the pressure-dependent resistance to microvoid-nucleation-induced shear localization which accelerates ductile fracture. Continuum mechanical models show the role of dispersion geometry (size, fraction, spatial inhomogeneity) and interfacial properties on microvoid nucleation and softening behavior. The models predict improved geometries for grain refining dispersions and allow estimates of particle interfacial properties from measured nucleation behavior as a basis of phase selection for optimal grain refining dispersions with maximum resistance to microvoid nucleation. For a given alloy composition and melt practice, procedures for optimization of solution treatment to eliminate unnecessary particles have demonstrated substantial toughness enhancement.

Controlled experiments defining austenite stability and critically testing the role of austenite in mechanical behavior show that conventional retained austenite is too unstable to enhance fracture toughness in ultrahigh-strength steels. Transformation kinetic theory prescribing the particle-size and composition dependence of dispersed austenite stability predicts that optimal stability for transformation toughening is achievable through austenite precipitation in high alloy steels. Guided by thermodynamic predictions, novel heat treatments and STEM microanalytical studies in AF1410 steel have demonstrated precipitation of

optimally stable ultrafine intralath austenite of near-equilibrium composition, yielding a record level of fracture toughness in this steel. Critical experiments in model austenitic alloys have identified an important role of transformation dilatation in the transformation toughening of ductile solids, providing a basis for design of superior alloy compositions for maximum dispersed-phase transformation toughening.

Thermodynamic and continuum mechanical modelling of the competition between intergranular separation and crack-tip blunting predicts a thermodynamic basis for intergranular hydrogen stress corrosion with support from available surface thermodynamic data. Directed at the electronic basis of the governing thermodynamic quantities, band theoretic and cluster model calculations for embrittling impurities in grain boundary and corresponding fracture surface environments show charge transfer, magnetic moment, and band structural changes which correlate with embrittlement potency. The emerging understanding of the electronic basis of embrittlement will allow design of grain boundary composition for both enhanced intrinsic cohesion and reduced hydrogen interaction, offering the greatest potential for property improvements. Substantial advances in hydrogen stress corrosion resistance through cleaning of impurities from grain boundaries have already been achieved by design of novel metastable impurity-gettering compounds accessible through rapid solidification processing.

Integration of these concepts within a systems engineering framework has led to the first demonstration of computer-aided thermodynamics-based design of a complex multicomponent alloy directed at specific property and microstructural objectives. The frontier of materials design defined by this research constitutes both a new concept of materials science and the advent of true materials engineering.

ACKNOWLEDGEMENTS

An initial phase of the Steel Research Group effort was conducted at MIT under NSF sponsorship. The expanded program now underway at Northwestern University is funded by NSF, ONR, NASA, ARO, AFOSR, and DOE, supplemented by industrial fellowship support. Coordinated efforts at Harvard and Brown Universities are supported by NSF.

REFERENCES

1. G.M. Jenkins, "The Systems Approach," in Systems Behavior, ed. J. Beishon and G. Peters, Open University Press, 1972.

2. C.S. Smith, A Search for Structure, MIT Press, Cambridge, MA, 1981.

3. M. Cohen, "Unknowables in the Essence of Materials Science and Engineering," Mat. Sci. and Eng. 25 (1976) 3.

4. M. Cohen, "Metallurgy and the Evolution of Materials Science and Engineering," these proceedings.

5. G.R. Speich, "Secondary Hardening Ultrahigh-Strength Steels," these proceedings.

6. G.R. Speich, D.S. Dabkowski, and L.F. Porter, Metall Trans. 4 (1973) 303.

7. J.A. Liddle, G.D.W. Smith, and G.B. Olson, "Alloy Carbide Precipitation in a High Cobalt-Nickel Secondary Hardening Steel," Proc. 33rd Int'l Field-Emission Symposium, J. de Physique, 47 (1986) C7-223.

8. J.S. Montgomery, and G.B. Olson, "Kinematics of M_2C Carbide Precipitation," these proceedings.

9. A.J. Allen, D. Gavillet, and J.R. Weertman, "SANS and TEM Studies of Isothermal M2C Carbide Precipitation in Ultrahigh-Strength AF1410 Steel," manuscript in preparation.

10. H. Wendt and P. Haasen, Acta Metall. 31 (1983) 1649.

11. R. Kampmann and R. Wagner, in Decomposition of Alloys, ed. P. Haasen et al., Pergamon Press, NY (1984) p. 91.

12. R. Wagner and R. Kampmann, "Solid State Precipitation at High Supersaturations," these proceedings.

13. J.S. Langer and A.J. Schwartz, Phys. Rev. A21 (1980) 948.

14. G.M. Carinci, G.B. Olson, J.A. Liddle, L. Chang, and G.D.W.Smith, "APFIM Study of Multicomponent Precipitation," these proceedings.

15. G.M. Carinci, "Precipitation of Multicomponent Carbides in Co-Ni Martensitic Steels," Ph.D. thesis, MIT, February 1989.

16. T. Kinkus and G.B. Olson, Northwestern University research in progress.

17. H.M. Lee, "Stability and Coarsening Resistance of M_2C Carbides in the Secondary Hardening Reaction," Ph.D. thesis, MIT, February 1989.

18. A.J. Garratt-Reed and H.M. Lee, MIT unpublished research, 1988.

19. M. Grujicic and G.B. Olson, CALPHAD 12 (1988) 405.

20. H.M. Lee, S.M. Allen, and M. Grujicic, "Stability and Coarsening Resistance of M_2C Carbides in Secondary Hardening Steels," these proceedings.

21. S. Bjorklund, L.F. Donaghey, and M. Hillert, Acta Met. 20 (1972) 867.

22. B. Sundman, B. Jansson, and J.O. Andersson, CALPHAD, 9 (1985) 153.

23. M. Grujicic, "Design of M_2C Carbides for Secondary Hardening," these proceedings.

24. K-U. King, P.W. Voorhees, T. Mura, and G.B. Olson, Northwestern University research in progress.

25. F. Larché and J.W. Cahn, Acta Metall. 21 (1973) 1051.

26. G. Ghosh and G.B. Olson, Northwestern University research in progress.

27. M. Schmidt and R. Hemphill, "Characterization of 4% Molybdenum SRG Experimental Steel," these proceedings.

28. R. Hemphill, Carpenter Steel alloy AerMet100, patent pending.

29. M. Grujicic and G.N. Haidemenopoulos, CALPHAD 12 (1988) 219.

30. J.L. Goss, "Austenitic Grain Growth and Precipitation Strengthening in Rapidly Solidified Alloys," M.S. thesis, MIT, August 1980.

31. J.J. Irani and R.W.K. Honeycombe, J. Iron and Steel Inst., 203 (1965) 826.

32. G.N. Haidemenopoulos, "Dispersed-Phase Transformation Toughening in Ultrahigh-Strength Steels," Ph.D. thesis, MIT, May 1988.

33. A.T. Davenport and R.W.K. Honeycombe, Metal Science, 9 (1975) 201.

34. S. Spooner, H.J. Rack, and D. Kalish, Metall. Trans. 2A (1971) 2306.

35. L. Chang, G.D.W. Smith, and G.B. Olson, J. de Physique 47 (1986) C2-265.

36. I. Aslanidis, "Softening and Recovery Resistance in Fe, Fe-Co, Fe-Al, Fe-Ni, and Fe-Ni-Co Alloys," Ph.D. thesis, MIT, September 1989.

37. V. Pierron-Bohnes, M.C. Cadeville, and G. Parette, J. Phys. F: Met. Phys., 15 (1985) 1441.

38. H. Warlimont and G. Thomas, Metal Sci. 4 (1972) 47.

39. S. Spooner, Oak Ridge National Laboratory, unpublished research.

40. A.F. Yedneral, O.P. Zhukov, M.A. Kablukovskaya, B.M. Mogutnov, and M.D. Perkas, Fiz. Metal. Metalloved, 36 (1974) 727.

41. A.B. Kuper, D. Lazarus, J.R. Manning, and C.T. Tomizuka, Phys. Rev., 104 (1956) 1536.

42. E. Hornbogen, "Alloy Design for >3GPa Steels," these proceedings.

43. C. Knepfler, K.T. Faber, and J. Weertman, Northwestern University, research in progress.

44. W.M. Garrison, Jr., and K.J. Handerhan, "Fracture Toughness: Particle-Dispersion Correlations," these proceedings.

45. G. Krauss, "Shear Fracture of Ultrahigh-Strength Low Alloy Steels," these proceedings.

46. J. Mescall and H. Rogers, "The Role of Shear Instability in Ballistic Penetration," these proceedings.

47. J.G. Cowie, M. Azrin, and G.B. Olson, "Microvoid Formation During Shear Deformation of Ultrahigh-Strength Steels," these proceedings.

48. J.G. Cowie, M. Azrin, and G.B. Olson, Metall. Trans. 20A (1989) 143.

49. M.J. Gore, "Grain Refining Dispersions and Mechanical Properties in Ultrahigh-Strength Steels," Ph.D. thesis, MIT, May 1988.

50. A. Benedetti and J.B. Cohen, Northwestern University, unpublished research, 1989.

51. A. Needleman, J. Applied Mechanics, 54 (1987) 525.

52. A. Needleman, "A Numerical Study of Void Nucleation at Carbides," these proceedings.

53. M.J. Gore, A. Needleman, and G.B. Olson, unpublished research, 1988.

54. J.W. Hutchinson and V. Tvergaard, "Effect of Particle-Void Interaction on Void Growth in Tension and Shear," these proceedings.

55. J.W. Hutchinson and V. Tvergaard, "Softening Due to Void Nucleation in Metals," in Fracture Mechanics: Perspectives and Directions ed. R.P. Wei and R.P Gangloff, ASTM STP 1020 (1989) p.61.

56. Y. Huang and J.W. Hutchinson, "A Model Study of the Role of Nonuniform Defect Distribution on Plastic Shear Localization," in Role of Modelling in Materials Design, ed. J.D. Embury, TMS-AIME (1990).

57. D.M. Tracey and P.J. Perrone, "Modelling of Interactions in Void Nucleation and Growth," these proceedings.

58. D.M. Tracey and P.J. Perrone, "Stress Distributions Near Microstructural Inhomogeneities,' Trans. 6th Army Conf. Applied Math. and Computing ARO Report #89-1 (1989).

59. M.J. Gore, G.B. Olson, and M. Cohen, "Grain-Refining Dispersions and Properties in Ultrahigh-Strength Steels," these proceedings.

60. C. Hayzelden, "Secondary Particle Dispersions and Impurity Gettering in Ultrahigh-Strength Steels," these proceedings.

61. R.J. Asaro and J.R. Rice, J. Mech. Phys. Solids 25 (1977) 309.

62. M. Schmidt and M.J. Gore, "Solution Treatment Effects in AF1410 Steel," these proceedings.

63. A.S. Argon and J. Im, Metall Trans., 6A (1975) 839.

64. J.H. Beatty and M. Azrin, MTL research in progress.

65. C-Y. Hsu, "Grain-Growth Mechanisms in Rapidly Solidified Matrix Steels," Ph.D. thesis, MIT, February 1984.

66. T. Gladman, Proc. R. Soc. A294 (1966) 298.

67. P. Hellman and M. Hillert, Scandinavian Journal of Metallurgy, 4 (1975) 211.

68. J.W. Flowers, Jr., and S.P. Karas, J. Appl. Phys. 38 (1967) 163.

69. T. Gladman and F.B. Pickering, JISI 205 (1967) 653.

70. L. Anand and J. Gurland, Metall Trans. 6A (1975) 928.

71. G.B. Olson and R.G. Bourdeau, "Rapidly Solidified Ferrous Alloys," in Rapidly Solidified Alloys, ed. S.K. Das, B.H. Kear, and C.M. Adam, TMS-AIME, Warrendale, PA (1985) p.185.

72. M.J. Gore, M. Grujicic, G.B. Olson, and M. Cohen, Acta Metall, 37 (1989) 2849.

73. G.B. Olson, "Transformation Plasticity and the Stability of Plastic Flow," in Deformation, Processing and Structure, chpt. 9, ed. G. Krauss, ASM (1984) p. 391.

74. G.B. Olson and M. Cohen, Metall. Trans. 13A (1982) 1907.

75. G.B. Olson and M. Cohen, Metall. Trans. 6A (1975) 791.

76. T. Narutani, G.B. Olson, and M. Cohen, J. de Physique 43 (1982) C4-429.

77. R.H. Leal, "Transformation Toughening of Metastable Austenitic Steels," Ph.D. thesis, MIT, June 1984.

78. G.B. Olson and M. Cohen, "Martensitic Transformation as a Deformation Process," in Mechanical Properties and Phase Transformations in Engineering Materials," ed.

S.D. Antalovich, R. O. Ritchie, and W.W. Gerberich, TMS-AIME (1986) p.367.

79. F. Stavehaug, "Transformation Toughening of γ'-Strengthened Metastable Austenitic Steels," Ph.D. thesis, MIT, June 1990.

80. R.G. Stringfellow and D.M. Parks, MIT research in progress.

81. G.N. Haidemenopoulos, G.B. Olson, M. Cohen, and K. Tsuzaki, Scripta Metall. 23 (1989) 207.

82. G.N. Haidemenopoulos, M. Grujicic, G.B. Olson, and M. Cohen, Acta Metall. 37 (1989) 1677.

83. G.N. Haidemenopoulos, G.B. Olson, and M. Cohen, "Dispersed-Phase Transformation Toughening in Ultrahigh-Strength Steels," these proceedings.

84. G.B. Olson and M. Cohen, "Dislocation Theory of Martensitic Transformations," in Dislocations in Solids, Vol. 7 ed. F.R.N. Nabarro, North-Holland, Amsterdam (1986) p. 295.

85. G.B. Olson, K. Tsuzaki, and M. Cohen, "Statistical Aspects of Martensitic Nucleation," Turnbull Symposium: Phase Transitions in Condensed Systems, ed. G.S. Cargill, F. Spaepen, and K.N. Tu, MRS (1987) p. 129.

86. I-W. Chen, Y-H. Chiao, and K. Tsuzaki, Acta Metall. 33 (1985) 1847.

87. M. Grujicic, M. Buonanno, S.M. Allen, G.B. Olson, and M. Cohen, "Heterogeneous Precipitation of Austenite for Stabilization," these proceedings.

88. B.V.N. Rao, "Ferrite-Austenite Dual Phase Steel," U.S. Patent 4,544,422, October 1, 1985.

89. C-C. Young, "Transformation Toughening in Phosphocarbide-Strengthened Austenitic Steels," Ph.D. thesis, MIT, May 1988.

90. B. Budiansky, J.W. Hutchinson, and J.C. Lambropoulos, Intl J. Solids and Structures, 19 (1983) 337.

91. G.N. Haidemenopoulos, M. Grujicic, G.B. Olson, and M. Cohen, CALPHAD 13 (1989) 215.

92. C. Kuehmann and G.B. Olson, Northwestern University research in progress.

93. C.J. McMahon, Jr., "Hydrogen Embrittlement of High-Strength Steels," these proceedings.

94. J.R. Rice and J-S. Wang, Mat. Sci. and Eng. A107 (1989) 23.

95. P.M. Anderson, J-S. Wang, and J.R. Rice, "Thermodynamic and Mechanical Models of Interfacial Embrittlement," these proceedings.

96. J-S. Wang, private communication.

97. E. Wimmer, C.L. Fu, and A.J. Freeman, Phys. Rev. Lett., 55 (1986) 2618.

98. R.J. Harrison, F. Spaepen, A.F. Voter, and S-P. Chen, "Structure of Grain Boundaries in Iron," these proceedings.

99. G.L. Krasko and G.B. Olson, "Evaluation of Decohesion Mechanisms by LMTO-ASA-Stoner Cohesive Energy Calculations," these proceedings.

100. G.L. Krasko and G.B. Olson, "The Effect of Boron, Carbon, Phosphorus and Sulfur on Intergranular Cohesion in Iron," submitted to Phys. Rev. B.

101. R.J. Harrison and G.L. Krasko, MTL research in progress.

102. G.L. Krasko and G.B. Olson, Phys. Rev B 40 (1989) 11536.

103. C. Li and A.J. Freeman, Northwestern University research in progress.

104. C.L. Briant and R.P. Messmer, Phil. Mag. B, 42 (1980) 569.

105. M.E. Eberhart and J.M. MacLaren, "Mechanisms for Cleavage and Intergranular Embrittlement in Fe," these proceedings.

106. H. Eguchi, "Electronic Basis of Phosphorus Embrittlement of Iron Grain Boundaries," M.S. thesis, Northwestern University, June 1990.

107. D.E. Ellis, "Molecular Clusters," in Handbook on the Physics and Chemistry of the Actinides, ed. A.J. Freeman and G.H. Lander, North-Holland, Amsterdam (1985) p.1.

108. J.F. Watton, G.B. Olson, and M. Cohen, "A Novel Hydrogen-Resistant UHS Steel," these proceedings.

109. G. Del Corso and G.B. Olson, unpublished research.

110. J.H. Graves and A.A. Anctil, MTL research in progress.

111. A. Bilyk, T. Chen, N. Akaiwa, H. Eguchi, and G.B. Olson, Northwestern University 750-C95 Materials Design Class Project Report, June 1989.

METALLURGY AND THE EVOLUTION OF MATERIALS SCIENCE AND ENGINEERING

MORRIS COHEN
Massachusetts Institute of Technology, Cambridge,
Massachusetts 02139

ABSTRACT

Materials have become increasingly ingrained in human existence ever since the emergence of mankind some hundred thousand years ago. The association between civilization and materials has intensified to the extent that, presently, about 15 billion tons of raw materials are taken annually from nature by mining, drilling, harvesting and fishing, to be converted into countless edifices, machines, devices, and products for societal purpose. Nevertheless, despite the magnitude and importance of this world-wide enterprise, often referred to as the global materials cycle, it has been only within the past thirty years that the field of materials has come into intellectual focus. This has been accomplished, in effect, by carrying over the central theme of metallurgy (namely, the interrelationships between the processing, structure, properties, and performance of the metallic state) to other classes of materials that are potentially accessible and useful to society. In other words, the discipline of metallurgy has provided an excellent paradigm for the newer and broader field of materials science and engineering (MSE), within which metallurgy has now become an indispensable part. However, the several disciplines which function within MSE have not yet blended sufficiently to operate as a unified branch of knowledge, and so MSE must still be viewed as a multidiscipline in a vibrant state of change. It will take time, perhaps another generation or two, for society to determine whether MSE can actually evolve into a coherent discipline unto itself -- in competition with other branches of knowledge which are striving for attention. The crucial test is likely to depend on two subtle criteria: How well will MSE aid the human mind to <u>understand</u> nature ever more thoroughly, and how well will MSE help society to <u>utilize</u> nature ever more wisely?

Conceptually, metallurgy and MSE have much in common.

In both cases, there is no clear separation between their scientific and engineering contents, and both gather special strength from this deliberate continuity. Both function most productively when there is an intimate mixing of scientific and experienced knowledge; yet major advances in this interplay are found to be initiated more frequently by novel processing and new experimental findings than by new theory. Hence, the hallmark of MSE thus far, as in metallurgy, is not the predictability of materials behavior from first principles, but the synergistic reciprocities which are discovered between processing and structure, structure and properties, properties and performance. The operations of these interrelationships are nicely illustrated by examples of recent advanced-material developments.

INTRODUCTION

Only a minuscule fraction of matter in the universe is accessible to earthlings for useful purposes as well as for study; this "fact of nature" highlights the distinction between matter in general and materials in particular. Thus, materials consist of those substances, both natural and man-made, that society can employ for producing things, e.g., edifices, machines, devices, tools, utensils, clothing, weapons, ornaments, and products of all kinds. From the perspective of history, materials such as wood, stone, fibers, ceramics, and metals have played an intimate role in the advance of civilization, and have become thoroughly ingrained not only in human existence, but also in the quality of life. Clearly, then, materials must be regarded as an essential working medium of society; they constitute one of the basic resources of the human race -- along with living space, food, energy, information, and manpower.

Inasmuch as materials thereby comprise an important part of the natural world that can be adapted to serve societal purposes, it is no wonder that social and intellectual forces are tending to pull various disciplines and subdisciplines into a coherent body of knowledge in order to reveal more about the character and utility of materials. What has emerged in this evolutionary transition is Materials Science and Engineering (MSE). In a rather natural way, the well-established discipline of metallurgy -- namely, the science and engineering of the metallic state -- has provided an appropriate paradigm for the newer and broader field of MSE, within which metallurgy now functions as a vital and exemplary component in coordination with other classes of materials. The field of ceramics, like metallurgy, has also reached the status of a discipline in its own right, and is now likewise recognized as a prominent component of MSE.

Before examining the significance of MSE in concept and in operation, it is well to visualize the scope of the overall materials enterprise.

THE GLOBAL MATERIALS CYCLE

Some 15 billion tons of raw materials (ores, minerals, coal, crude oil, natural gas, rock, sand, timber, rubber, etc.) are extracted annually from natural sources by mining, drilling, and harvesting from land and sea, to be processed into bulk and engineering materials (metals and alloys, ceramics and glass, chemicals, cement, lumber, dielectrics, semiconductors, plastics and elastomers, paper, composites, etc.) for fabrication into articles of commerce in response to societal demand. In due course, after these materials have played out their respective functions in service, they are discarded as scrap, either to be recycled for use again and again, or somehow returned to nature whence they came. Accordingly, the total materials system is a cradle-to-grave circuit on a global scale, involving interdependence as well as competition among countries and companies. It is evident that this global materials cycle -- so named by the COSMAT Report of 1974(1) -- participates significantly in the foreign and domestic affairs of nations for both economic and strategic reasons. That study found, for instance, that the materials cycle accounts for about one-fifth of the gross national product together with one-fifth of the human employment in the United States, not including the production of food and fuel.

The materials cycle is driven by societal demand, with value being added progressively to the materials-flow around the circuit. A substantial portion of this added value is in the form of energy. Approximately one-half of the energy consumed by manufacturing industries in the United States is expended in the production, refining, fabrication, and assembly of materials into end-products. Conversely, materials are necessary for supplying energy in useful form. In addition to the indispensability of fuel materials for generating energy, virtually all advanced energy-conversion technologies are presently materials-limited from the standpoint of efficiency, reliability, safety, or cost-effectiveness. This is the case, for example, with gas turbines, nuclear reactors, solar-energy devices, magnetohydrodynamics, high-energy batteries, and fuel cells.

The flow of materials in the materials cycle can be greatly perturbed at any given point by economic factors (e.g., competitiveness), political actions (e.g., embargoes), or social decisions (e.g., environmental regulations), which may take place elsewhere in the world. Shortages in materials are usually due to such man-made disruptions rather than to global scarcities in natural sources. It should also be recognized that the operation of the materials cycle inevitably taxes the environment through waste disposal, pollution, and landscape disfigurement, thus impacting the availability of clean living space and injecting real, but hard-to-assess, social costs. These are major issues which must be faced by those concerned with the overall human benefits to be derived from MSE. Metallurgy has had to cope with this problem for many decades.

THE NATURE OF MSE

Materials science and engineering comprises a mixture of disciplines (branches of knowledge) that provide an intellectual approach for dealing with materials as a part of nature, and for harnessing them to human purpose. The aforementioned COSMAT Study(1) arrived at the model of MSE illustrated in Fig. 1. It is a knowledge-generation and knowledge-transfer system which extends from basic science

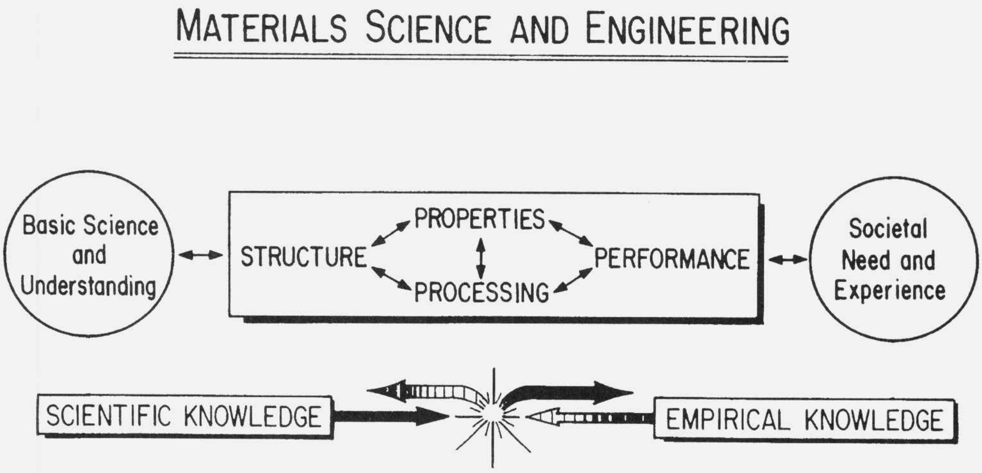

Figure 1. A model of materials science and engineering, indicating countercurrent flows of scientific and empirical knowledge relative to materials. Based on COSMAT Report of 1974(1).

and fundamental understanding (on the left) to societal needs and experience (on the right). MSE attempts to relate the processing of materials (including their synthesis, specimen preparation for research, large-scale production in the materials cycle, and fabrication for end-use) to their inner architecture (comprising all levels of structure and composition) and their manifested properties (of all relevant types), and then to their ultimate performance in service applications. COSMAT defined MSE more succinctly but in similar terms: "MSE is concerned with the generation and application of knowledge relating the composition, structure, and processing of materials to their properties and uses." Metallurgy has functioned in this way for over a hundred years, since the momentous disclosure of microstructure, whereas MSE came into being in this mode only some thirty years ago.

Materials science and engineering is holistic in the sense that it emphasizes a continuity in the field of materials between science, engineering, technology, and the requirements of society; as such, it exposes mankind to the opportunities opened up by fundamental knowledge concerning materials, and conversely, it exposes scientific theory and experimentation regarding materials to the demands and experience of mankind. In fact, MSE operates most effectively for discovering and applying new processes and materials when the countercurrent flows (indicated in Fig. 1) of scientific knowledge gained from research and empirical knowledge acquired from experience are so intimately mixed that each catalyzes the other. Thus far, MSE has not replaced or eliminated any of the disciplines or subdisciplines that contribute to it. Instead, MSE acts as a multidisciplinary arena for all branches of knowledge that can shed light on materials. In so doing, MSE promotes new interactions and interdisciplinary objectives that are not otherwise fostered among the separate disciplines.

Case studies of selected materials innovations have been described in considerable detail(2), covering metallic, ceramic, polymeric, and electronic materials. Generally speaking, these advances were initiated by societal "pull" rather than by scientific "push," although science was invariably brought to bear in the progress toward successful utilization. Even the oft-cited transistor "break-through" -- which emanated so spectacularly from brilliant theory, basic research, and novel processing -- was actually first inspired (at the Bell Telephone Laboratories) by a perceived societal need to move well beyond the existing vacuum-tube technology in order to achieve more complex switching and multichannel transmission circuitry for future communication systems. This is a particularly revealing example of the synergistic interplay between experience and scientific findings in MSE. It is a functional style that characterizes the way MSE works, but it has long been exemplified in the operation of metallurgical science and engineering.

More recent examples in MSE continue to be consistent with this theme. Figure 2 portrays the "quantum" advances that have been attained in strong permanent magnets, notably in the discovery of the $Nd_2Fe_{14}B$-type intermetallic compounds and their appropriate processing(3). This development resulted from experimental research and societal pull; no theory was on hand to predict such magnetically strong compounds or to guide their improvement. Undoubtedly, the necessary theoretical work will be forthcoming in time and

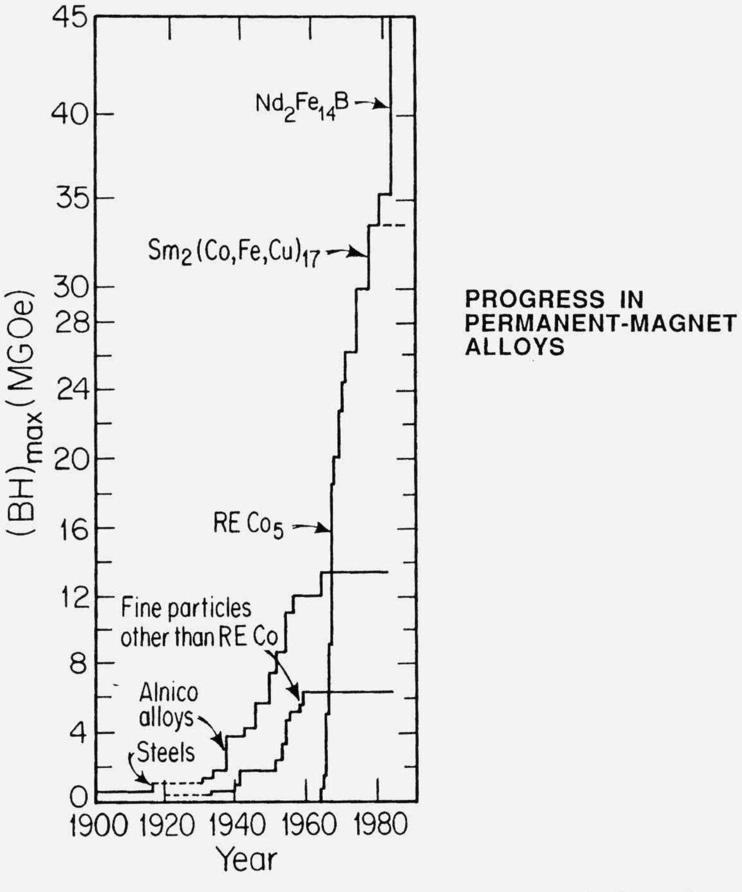

Figure 2. Advances in permanent-magnet materials since the year 1900, according to the energy product $(BH)_{max}$ as a figure of merit. From NMAB Report of 1985(3)

will contribute quite beneficially to both the understanding and the further progress of these technologically important materials, but MSE and society do not have to wait for that desirable occurrence. One can already see that this materials advance is likely to exert a major influence on new motor and electronic device designs, featuring greater efficiencies and miniaturization.

The dramatic discovery of high-temperature superconductivity in layered copper oxides, more specifically $(La,Sr)_2CuO_4$ and $YBa_2Cu_3O_x$, offers another case in point, as denoted by the striking increase of the critical temperature (T_c) in Fig. 3(4). Here again, there was no theory even to

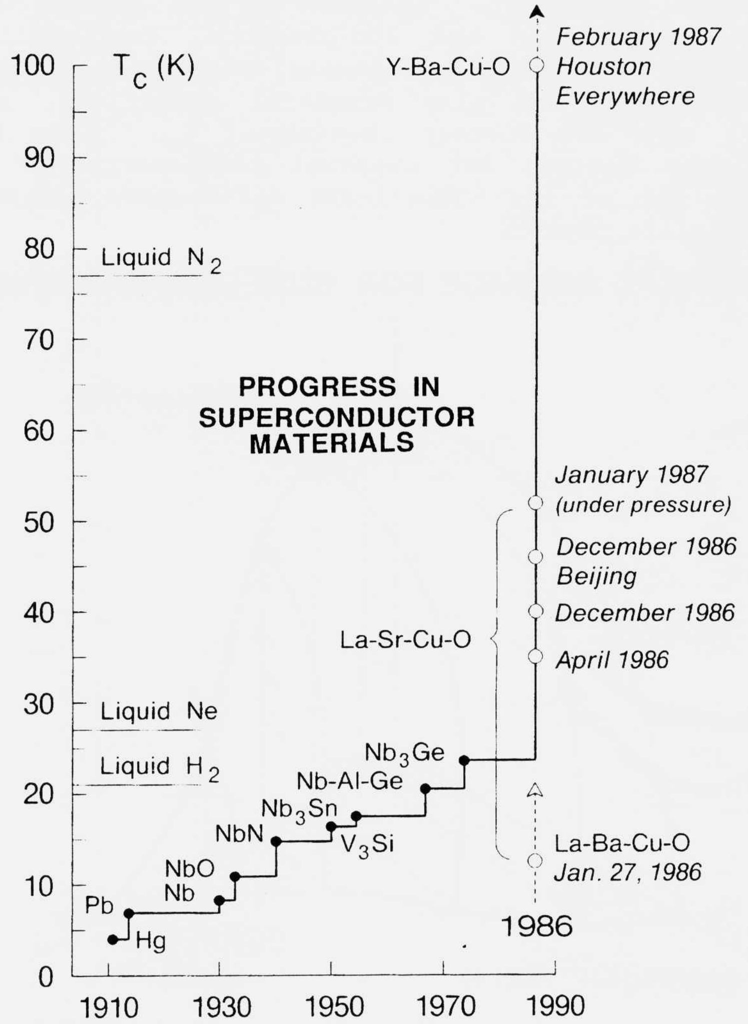

Figure 3. Advances in the critical temperature (T_c) for superconductivity. From compilation of Muller and Bednorz(4).

hint at, let alone predict, this astonishing solid-state behavior. Indeed, the ensuing burst of excitement throughout the world has been due not only to the prospect of revolutionary new technologies (the societal pull), but also to the demonstrated inadequacy of existing theory for a physical property as noteworthy as superconductivity. And yet, in view of the very nature of MSE, experimental research on the associated processing/structure/property relationships in these ceramic materials is proceeding apace, with due attention to the combined effects of temperature, magnetic field, and current density for accessing and stabilizing the superconducting state of candidate materials, as suggested by Fig. 4(5). Furthermore, inasmuch as MSE carries over to materials performance and end-products, fabricability to useful shapes and suitable mechanical properties to withstand service stresses are also essential objectives, no less important than any further raising of T_c. This need to balance many factors for eventual performance in service highlights one of the significant differences beteween MSE and solid-state physics.

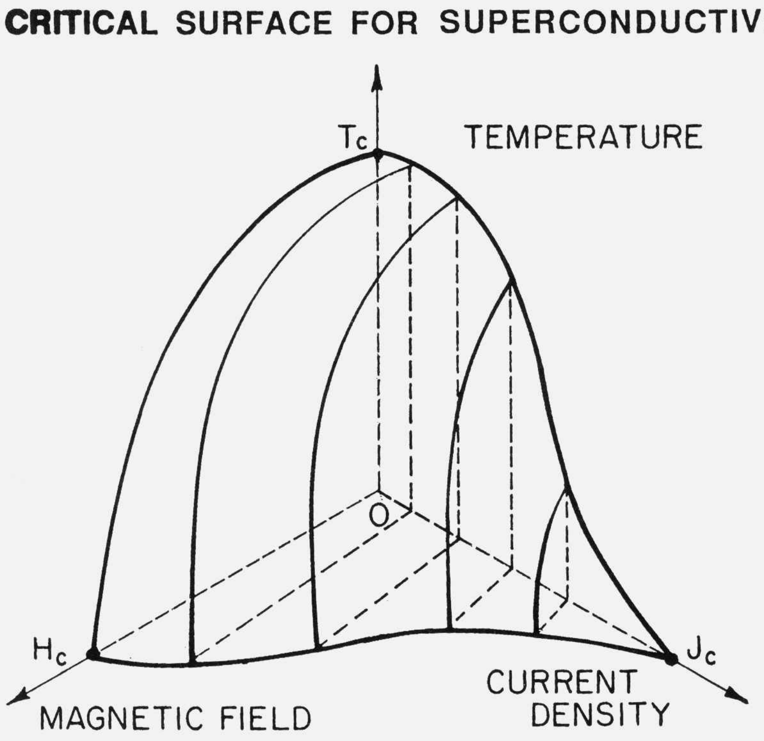
CRITICAL SURFACE FOR SUPERCONDUCTIVITY

Figure 4. Interplay of temperature, magnetic field, and current density in defining the regime of superconductivity. After Livingston(5).

PREDICTABILITY VERSUS RECIPROCITY IN MSE

In MSE, one would ideally like to use the structure of materials to predict properties, then to use properties to predict performance, and finally to select a sequence of processing procedures that will yield the desired material and inner structure at a reasonable cost. However, there is much that interferes with this simple logic, in view of the deliberate continuity of science and engineering in MSE. The properties which enable materials to perform their respective assignments in service, and in harmony with the diverse functions of their companion materials, are numerous and complex, and they must also manifest themselves satisfactorily under the multidimensional requirements of the designated application. There is just no way of itemizing all of the operating and environmental variables for complete property simulation in the laboratory; moreover, the properties that can be measured will, at best, be only simple images of what may be at play in service performance.

In a real sense, then, materials behavior in service is unknowable from properties alone(6). Properties can offer valuable guidance when combined with accumulated experience, but one would not expect to rely on prediction in the first instance, no matter how accurately the measurable properties might be known. As with a musical instrument, no one can truly deduce how well it will perform until it is actually played! Indeed, empirical knowledge is often needed first in order to decide just which properties should be evaluated to correlate with performance. It is not predictability but mutual reciprocity between properties and performance (with each reinforcing the other in a symbiotic interplay) that participates so successfully in the practical output of MSE. In line with the MSE model of Fig. 1, we are referring here to a purposeful intermixing between scientific experimental knowledge relating to selected properties (mechanical, chemical, electrical, etc., as the case may be) and empirical knowledge arising from service experience.

Similar reasoning applies to structure/property relationships. Much of the science in MSE is directed to explanations of the observed properties of materials in terms of their internal structure. Such linkages are typically made through theories, models, or assumed mechanisms. However, the very idea of structure encompasses many levels of fine-scale entities or "building blocks" nesting together in hierarchies of regularities and irregularities. The schematic structure of a macromolecular composite material in Fig. 5 --

specifically a tendon which connects muscle and bone in humans and animals -- is particularly instructive; it illustrates several hierarchical levels, together with their respective size scales, nomenclature, and methods of detection(7). The many kinds of interfaces in Figure 5 must also be considered as important property-influencing elements of the structure. And not shown here are still finer constituents such as molecules, atoms, electrons, and ghost-like particles ranging on and on down through the subnuclear hierarchies until comprehension is exhausted. Under these circumstances and in the context of MSE, one must surely question whether it will ever be possible to predict from

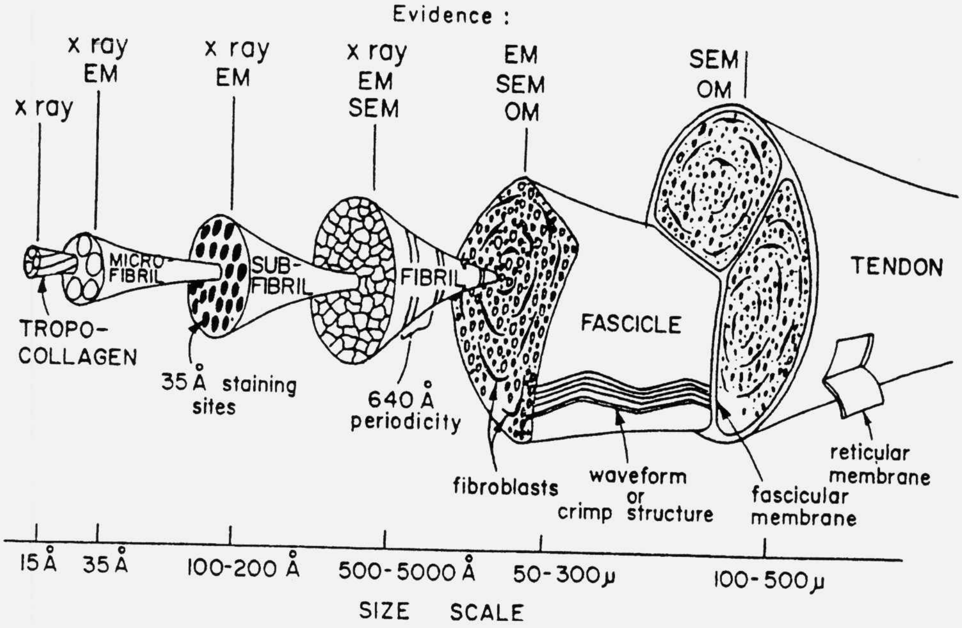

Figure 5. Schematic illustration of the hierarchical structure of a biological material (tendon), showing size scales, terminology, and methods of observation. Abbreviations: DSC - differential scanning calorimetry; EM - electron microscopy; SEM - scanning electron microscopy; OM - optical microscopy. From Kastelic et al.(7)

first principles, or from structure alone, the relatively intricate properties that make materials useful to mankind. Fortunately, MSE can avoid this profound issue by depending on the mutual reciprocity between internal structure and measured properties, and not on a first-order predictability of one from the other. Again, MSE promotes a synergistic mixing of scientific and empirical information -- with structure and properties contributing, each in its own way, to a deeper and more helpful understanding of both.

It becomes evident that in its comparatively brief existence MSE has taken on the back-and-forth information-transfer features which have successfully evolved in metallurgy ever since, over a century ago, Henry Clifton Sorby opened up the science of metallography by revealing the microstructure of polished-and-etched iron and steel with the petrographic microscope(8). Plainly,the ultimate conversion of scientific understanding into societal well-being via MSE cannot be represented by a one-way stream of knowledge into practice; it depends more on turbulent, mutually interactive flows among the MSE components of processing, structure, properties, and performance. MSE seems to function most effectively as a dynamic system of knowledge generation and utilization when its elements are closely coupled and are also subjected to the stimulating and biasing forces of human needs.

AN EXAMPLE OF MSE IN OPERATION: RAPID SOLIDIFICATION PROCESSING

In MSE as well as in metallurgy, advances in structure/property relationships -- and likewise in the development of new materials -- are often crucially dependent on the emergence of novel processing methods. One such instance is rapid solidification processing.

With certain alloy systems, cooling rates of 10^4 - 10^6 degrees per second from the liquid state can avoid crystal nucleation, or solidification in the ordinary sense, and this results in the formation of metastable noncrystalline solids, otherwise termed metallic glasses. This phenomenon has been known since 1960 when the innovative experimental technique of splat quenching was introduced(9). It led to intensive scientific study of the structure and properties of metallic glasses, and at the same time it stimulated the development of larger-scale rapid solidification processes such as melt spinning for thin-strip casting and atomization for powder making. Correspondingly, much attention of a scientific nature was directed to the kinetics of solidification under conditions of rapid cooling and supercooling.

With regard to property measurements, it was found that iron-boron-silicon and iron-boron-silicon-carbon amorphous solids are not only ferromagnetic but also exhibit very low hysteresis and eddy-current losses, primarily due to their high electrical resistivity as well as their relative freedom from magnetocrystalline anisotropy and from microstructural defects normally associated with the crystalline state. The prevailing societal pull for saving energy, in this instance through decreased core-losses in electric transformers, provided a strong driving force for further process and alloy development based on these metallic glasses. The ensuing improvement in core-loss reduction is shown in Fig. 6, comparing the new amorphous materials with the more familiar silicon steels(10). The 60-Hz core losses of the metallic glasses going into the service testing of distribution transformers are less than one-third of the best silicon steels, and further reductions to one-twentieth have been achieved(10).

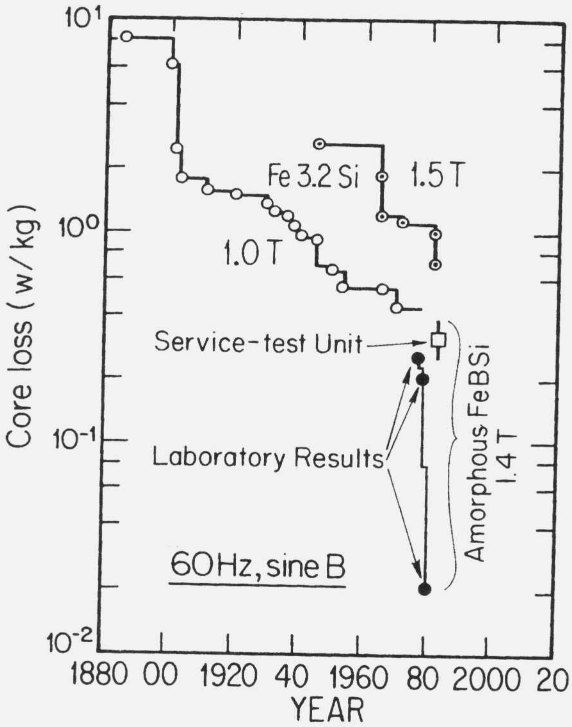

Figure 6. Advances in the reduction of core-losses in electric-transformer materials during the past century. From Luborsky(10).

In the operation of MSE, it will be obvious that the effective utilization of metallic glasses in transformers depends not only on favorable magnetic properties, but also on mechanical behavior, formability, stability versus time and temperature, and, of course, on the overall economics. Such interacting factors can only be resolved and optimized by promoting a close interplay of scientific and empirical findings. It has been reported that the performance tests on the subject transformers have demonstrated improved service as expected, and valuable additional information has been accumulated. Actual production is now under way. Core losses in distribution transformers alone in the United States are estimated to represent a wastage of three-quarters of a billion dollars annually, of which approximately one-third can be saved by using the metallic glass cores(10). Opportunities for the still-larger power transformers lie ahead, while many applications for amorphous alloys in smaller magnetic devices are already at hand.

This example of a materials advance serves to illuminate the way in which novel processing methods can stimulate the detailed study and development of previously unavailable materials and, in turn, lead to new technologies and products for filling the needs of society.

When rapid solidification processing is directed to crystalline materials, a wide diversity of microstructures, not otherwise attainable, can be accessed. This includes microstructural refinement of the matrix phase, unusual dispersions of embedded precipitates, high degrees of solid-solution supersaturation, and formation of metastable states. The dispersed particles are of special interest here because they are extremely fine, well distributed, and can have very limited solubility in the matrix phase. Because of the latter circumstance, the dispersed precipitates resist coarsening at high temperatures, and so tend to remain effective in pinning grain boundaries for inhibiting grain growth during subsequent thermomechanical treatments. For similar reasons, dispersion strengthening tends to be maintained at elevated temperatures. Moreover, rather large volume fractions of the dispersed phases are obtainable because the prior "solutionizing" is carried out in the liquid state, and precipitation into unduly coarse embrittling inclusions on cooling is avoided by the rapid solidification process.

Rapid solidification by nitrogen-gas atomizing for achieving uniform dispersions of the primary carbides in high-speed steels has been in industrial practice since 1970(11), benefiting from improved toughness at high hardness levels.* However, with the later innovation of centrifugal

---

*When particulates are produced in rapid solidification processing, consolidation into bulk materials is typically accomplished by powder-metallurgy techniques such as hot extrusion and hot isostatic pressing.

atomizing(12) and its potential for advanced superalloys, the U.S. Air Force became intrigued with the wider prospects for aerospace applications and initiated funding for more broadly-based research and development on new alloy systems, thus exemplifying another classic instance of societal pull in action. Because of the ultrafine-scale structures to be investigated, a need arose for the most sophisticated high-resolution electron microscopy and microanalytical instrumentation, and there erupted a spontaneous urge for scientific inquiry. Mutually stimulating interactions throughout the materials knowledge-transfer system of Fig. 1 came into play, rebounding dynamically among scientific explanation, property enhancement, process improvement, and high-technology performance, while concomitantly inspiring the joint participation of governmental, industrial, and academic institutions.

Some property results on rapidly solidified aluminum alloys are summarized in Fig. 7(13). Unusual ranges of composition and exceptional dispersions of intermetallic phases

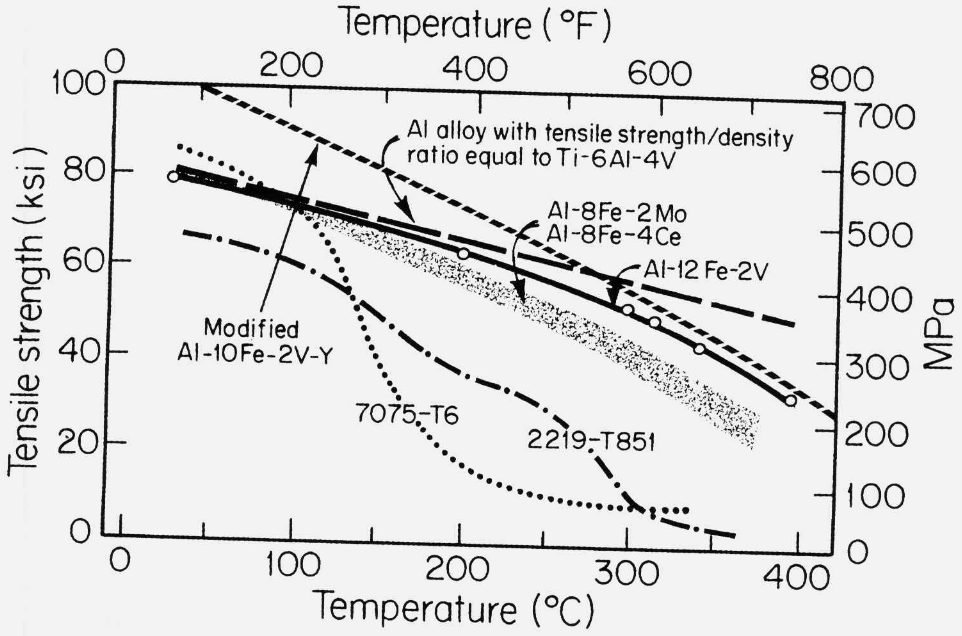

Figure 7. High-temperature strength of rapidly solidified aluminum-iron-base alloys, compared to two conventionally processed high-strength aluminum alloys (7075-T6 and 2219-T851). Dashed line denotes strength required of aluminum alloys to have the same density-compensated strength as a commercial titanium alloy. From Adam and Lewis(13).

are made possible by rapid solidification. The advantageous strength-retention at elevated temperatures shown in Fig. 7 for this class of materials is a consequence of the resistance to coarsening of the relatively stable dispersed phases. It is significant to note that, on a density-compensated basis, some of these aluminum alloys now equal or exceed the high-temperature strength of titanium alloys. These aluminum alloys also exhibit marked resistance to saline corrosion (Fig. 8), which probably arises from the alloy chemistry and microstructural uniformity attainable by rapid solidification(13).

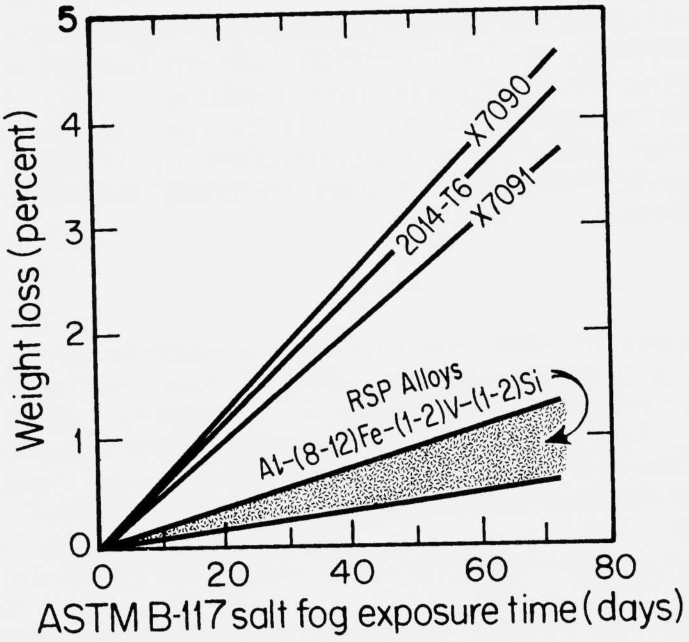

Figure 8. Corrosion resisance of rapidly solidified aluminum-iron-base alloys, compared to three conventionally processed aluminum alloys. From Adam and Lewis(13).

Up to the present time, the cost of rapid solidification processing has tended to channel its commercial use toward high-value-added end-products that may not yet be in the public domain. But it is clear that the underlying features of MSE are at work.

CLOSURE

Through the operation of the materials cycle on a global scale, materials now constitute a basic resource of society that not only connects peoples and governments on this planet, but also joins mankind into a partnership with nature. The high purpose of MSE is to help advance human understanding of nature by probing its materials thoroughly, and concurrently to help mankind live in harmony with nature by employing its materials intelligently. This dual objective, both intellectual and utilitarian, forms an integral part of the overarching contributions of science and engineering toward the general goal of human betterment and social progress.

At present, MSE functions as a mixture of disciplines, i.e., as a multidiscipline, rather than as an individual branch of learning like physics, chemistry, metallurgy, or ceramics. Of course, these disciplines originally did not enjoy sufficient coherence or identity to be recognized by society as unified fields of inquiry and endeavor. When such recognition does happen to emerge, it usually signals a recodification or repackaging of knowledge by society, and is characteristically reflected in the advent of university departments, curricula, degrees, job titles, technical societies, and professional groupings. This state of cohesion has not yet been decisively reached by MSE, but events are certainly moving in that direction. MSE has already established sufficient integrity to provide an attractive framework for newer classes of materials coming on the scene. Indeed, it is no longer likely that polymeric, electronic, photonic, and biological materials will form separate disciplines by themselves, as was the case earlier for metals and ceramics. It may take another generation or two for society to determine whether the various fields of knowledge that contribute to MSE will converge into a single discipline unto itself. An interesting example of this kind of evolutionary change is the field of medicine, which became a recognized discipline in spite of its many disparate specialties and subdisciplines. MSE can attain a similar stage of intellectual and professional cohesion by demonstrating to society that it provides a new challenge for studying nature deeply and for using nature wisely.

In the meantime, MSE is passing through a vibrant period of ferment and wondrous change. Knowingly or unknowingly, a substantial part of the world's technical community is caught up in it; and human well-being everywhere depends on it.

Acknowledgments

The author is immensely grateful to The Inamori Foundation of Kyoto, Japan for inviting this paper as a Commemorative Lecture on the occasion of awarding the 1987 Kyoto Prize. Sincere appreciation is also due to Marguerite Meyer, Lois Malone, Miriam Rich, and John Mara, all of MIT, who helped unsparingly in the preparation of the manuscript. Professor Eric Baer of Case Western Reserve University was kind enough to furnish Figure 5 for its reproduction here. And special recognition must be given to the Office of Naval Research and the National Science Foundation for their long-range support of the author's research and that of his students over many years at MIT.

References

1. COSMAT Summary Report, "Materials and Man's Needs," National Academy of Sciences, Washington, DC (1974). See also "Materials Science and Engineering: Its Evolution, Practice and Prospects," M. Cohen, Ed., Mater. Sci. and Eng. 37, No. 1 (Jan. 1979), including papers by M. Kranzberg and C. S. Smith, "Materials in History and Society," Part I, p. 1; and R. S. Claassen and A. G. Chynoweth, "Materials Science and Engineering as a Multidiscipline," Part II, p. 41.

2. COSMAT Supplementary Report, Vol. I, "The History, Scope, and Nature of Materials Science and Engineering," National Academy of Sciences (1975). See also R. S. Claassen and A. G. Chynoweth, "Materials Science and Engineering as a Multidiscipline," Mater. Sci. and Eng., 37 No. 1 (Jan. 1979) p. 51.

3. "Magnetic Materials," MNAB Report No. 426, Committee on Magnetic Materials, National Materials Advisory Board, National Academy Press, Washington, DC (1985).

4. K. Muller and J. G. Bednorz, "The Discovery of a Class of High-Temperature Superconductors," Science, 237 (4 Sept. 1987) p. 1133.

5. J. D. Livingston, "Superconducting Materials: Metallurgy," Encyclopedia of Materials Science and Engineering, M. B. Bever, Ed., Pergamon Press, Oxford and MIT Press, Cambridge (1986).

6. M. Cohen, "Unknowables in the Essence of Materials Science and Engineering," Mater. Sci. and Eng., 25 (1976) p. 3.